Aerospace Science and Technology 168 (2026) 110947

Contents lists available at ScienceDirect

Aerospace Science and Technology

journal homepage: www.elsevier.com/locate/aescte

Nonlinear aerodynamic flutter responses of the composite pipes conveying two-phase flow using mathematical simulation and data-driven solution

Yujun Cao [a,*], Mohammed El-Meligy [b,c], Mubariz Garayev [d]

[a] School of Engineering Science, Shandong Xiehe University, Jinan 250107, PR China
[b] Jadara University Research Center, Jadara University,PO Box 733, Irbid, Jordan
[c] Applied Science Research Center, Applied Science Private University, Amman, Jordan
[d] Department of Mathematics, College of Science, King Saud University, P.O Box 2455, Riyadh, Saudi Arabia

ARTICLE INFO

Communicated by Cummings Russell

Keywords:
Aerodynamics
Aeroelastic control
Two-phase flow
Non-linear dynamics
Functional graded material
Data-driven solution

ABSTRACT

Two-phase flows are encountered in a wide range of engineering systems, including nuclear reactors, thermal power plants, chemical reactors, petroleum pipelines, refrigeration systems, and aerospace propulsion systems. The ability to model and analyze two-phase flows is essential for the design, operation, and optimization of these systems. So, in this work, for the first time, nonlinear aerodynamic responses of pipe conveying two-phase flow using data-driven solutions in the mathematical framework are presented. The presented pipe system is made of triply periodic minimum material with exceptional mechanical properties, such as high specific strength, specific stiffness, and energy absorption qualities. The distribution parameter varies as a function of the two-phase Reynolds number in a pipe while keeping the void percent constant and modifying the density ratios. Nonlinear Von-Karman theory, as well as trigonometric shear deformation theory, is presented to correctly simulate the nonlinear aerodynamic responses of the pipe reinforced by triply periodic minimum material conveying two-phase flow. After that, a numerical solution procedure is used to solve the nonlinear governing equations with the aid of nonlinear boundary equations. After obtaining the dataset using the mathematical modeling section, the data-driven solution is used to correctly test, train, and validate results for simulating the current applicable structure in other complex situations. The proposed data-driven solution provides valuable insights into the nonlinear aerodynamic responses of the reinforced pipes, facilitating the design and optimization of robust and efficient piping systems for various engineering applications.

Nomenclature

Symbol	Definition	Units	Equation/ Table
A_G, A_L	The cross-sectional area occupied by gas/ liquid	m^2	Eq. 5
A_P	Inner pipe cross-sectional area	m^2	Eq. 5
C_0	Distribution parameter	-	Eq. 9
D_h	Hydraulic diameter	m	Eq. 6
E^m, E^{TPMS}	Young's modulus	Pa	Table 1
G^m, G^{TPMS}	Shear modulus	Pa	Table 1
K_w	Winkler foundation stiffness of the auxetic foundation	N/m^3	Eq. 20
L	Pipe length	m	Fig. 1
M_2, M_3	Drift velocity correction factors	-	Eqs. 7a-b
M_∞	Mach number	-	Eq. 22
Re_{tp}	Two-phase Reynolds number	-	Eq. 10
R_i, R_o	Pipe inner/outer radius	m	Fig. 1
V	TPMS volume ratio	-	Eq. 3
V_f	Mixture flow velocity	m/s	Eq. 6
V_G, V_L	Gas/liquid phase velocity	m/s	Eqs. 8, 11
V_{GM}	Gas drift velocity	m/s	Eq. 6
V_z	Thickness-dependent volume function	-	Eq. 4
ϵ_G	Gas void fraction	-	Eq. 5
γ_{xz}, $\gamma_{\theta z}$	Shear strains	-	Eqs. 13b, 14e-f
ε_{xx}, $\varepsilon_{\theta\theta}$	Normal strains	-	Eqs. 13a, 14a-b
λ_∞	Aerodynamic pressure parameter	-	Eq. 23
μ	Mass ratio	-	Eq. 23
ν^m, ν^{TPMS}	Poisson's ratio	-	Table 1

(continued on next column)
(continued)
(continued on next page)

* Corresponding author.
E-mail address: yujun_cao@163.com (Y. Cao).

https://doi.org/10.1016/j.ast.2025.110947
Received 20 January 2025; Received in revised form 7 September 2025; Accepted 15 September 2025
Available online 17 September 2025

(*continued*)

ρ_G, ρ_L	Gas/liquid density	kg/m^3	Eq. 6
ρ_∞	Free-stream air density	kg/m^3	Eq. 22
σ_{xx}, $\sigma_{\theta\theta}$	Normal stresses	Pa	Eqs. 15a-b
$\tau_{x\theta}$, $\tau_{\theta z}$	Shear stresses	Pa	Eqs. 15d
ψ	TPMS surface function	-	Eqs. 1a-c
DNN	Deep Neural Network	-	Abstract
DQA	Differential quadrature approach	-	Section 3.1
FG	Functionally graded	-	Section 2.1
PA /*PB*	Volume distribution patterns (Power /Trigonometric) of *TPMS*.	-	Eq. 4
TPMS	Triply Periodic Minimal Surface	-	Section 2.1
Ω_R	Real part of natural frequency	Hz	Eq. 37
Ω_I	Imaginary part of natural frequency	Hz	Eq. 37

1. Introduction

The analysis of two-phase flow-induced vibrations in aerospace piping systems is critical for structural reliability, as demonstrated by turbopump feedlines in rocket engines like SpaceX's Raptor experiencing dangerous flutter during cryogenic propellant transfer [1]. Similar challenges occur in aircraft fuel jettison systems, where Boeing 787 vent pipes suffer from destructive pressure pulsations caused by air-fuel mixture dynamics [2]. Spacecraft thermal control systems, such as the ISS ammonia cooling loops, face operational risks from two-phase flow instabilities during phase-change processes in microgravity conditions [3]. Hypersonic vehicles like DARPA's HTV-2 encounter even more severe aerothermal flutter in scramjet coolant channels due to supercritical fluid transitions at extreme velocities [4]. Rocket engine Turbopump feedlines schematic view in real and modeling [5,6] is shown in Fig. 1.

In recent times, there has been significant interest in lattice frameworks because of their exceptional mechanical properties, such as high specific strength, specific stiffness, and energy absorption qualities [7–9]. Conventional architectures are unable to provide the lightweight, adjustable, and flexible qualities of the lattice structure. Lattice structures have expanded their potential applications in automotive, civil, aircraft, civil, robotics, and other fields [10,11].

Triply periodic minimal surface (TPMS) materials are revolutionizing engineering design due to their unique combination of structural efficiency and lightweight properties [12,13]. These materials are characterized by their intricate, repeating geometries that minimize surface area while maintaining mechanical strength [14]. Engineers leverage TPMS structures in diverse applications, including aerospace, biomedical implants, and energy systems, where optimized material usage is critical [15]. Their high surface-to-volume ratio and tunable porosity make them ideal for heat exchangers and filtration systems, enhancing performance and efficiency [16]. The mathematical precision underlying TPMS designs allows engineers to create highly customizable and scalable solutions for specific industry challenges [17]. Additive manufacturing technologies, such as 3D printing, have further unlocked the potential of TPMS materials, enabling complex geometries that were previously unattainable [18]. By studying the mechanical and thermal behaviors of TPMS structures, engineers can develop innovative solutions that balance durability and functionality [19]. Furthermore, these materials open new avenues for sustainable engineering by reducing material waste and improving resource efficiency [20].

Pipes are extensively utilized in various industries such as petroleum engineering [21], chemical industry [22], nuclear engineering [23], and other industries [24]. Excessive vibration generated by the fluid being conveyed might result in pipe or pipe fitting breakdown, leading to substantial losses. Therefore, it is crucial to investigate the vibration and control of pipe systems utilized for fluid transportation [25]. Studying the mechanism and significant elements of vibration caused by gas-liquid flow in pipes is both theoretically important and practically applicable in engineering. It is essential for maintaining the secure and dependable functioning of boilers that generate steam in nuclear generation plants, heat exchangers that handle two-phase flow, and systems used for transporting oil and gas.

The fundamental mathematical formulas of motion can succinctly express the basic dynamics of pipe systems. However, the complex and dynamic behavior observed in these systems justifies the need for additional scholarly investigation [26]. For instance, the works of Ibrahim in 2010 and 2011 provide extensive knowledge on various modeling techniques, dynamic analysis, and equilibrium states of flow transfer pipes that confront both elastic and inelastic impediments. This comprehensive study explores the complex issues of fluid transfer pipelines, specifically focusing on the challenges related to their dynamic behavior and stability when subjected to different boundary conditions. Furthermore, the study investigates the phenomenon of fluid elastic instability in both single-phase and two-phase flows and thoroughly analyzes the occurrence of micromotion wear in crucial process equipment, such as heat exchangers and steam generators. In their study, Liu et al. [27] discovered that the strength of the gas-liquid two-phase force is directly proportional to the average velocity of the gas-liquid two-phase flow.

The high pressure in the pipe will result in a higher density of the gas phase due to its compressibility. This leads to a decrease in momentum flux that is less significant compared to low-pressure pipes, resulting in relatively fewer oscillations in high-pressure pipes. Ref. [28] observed that in slug flow and churn flow, there are significant fluctuations in the density of the mixture, resulting in major variations in momentum flux

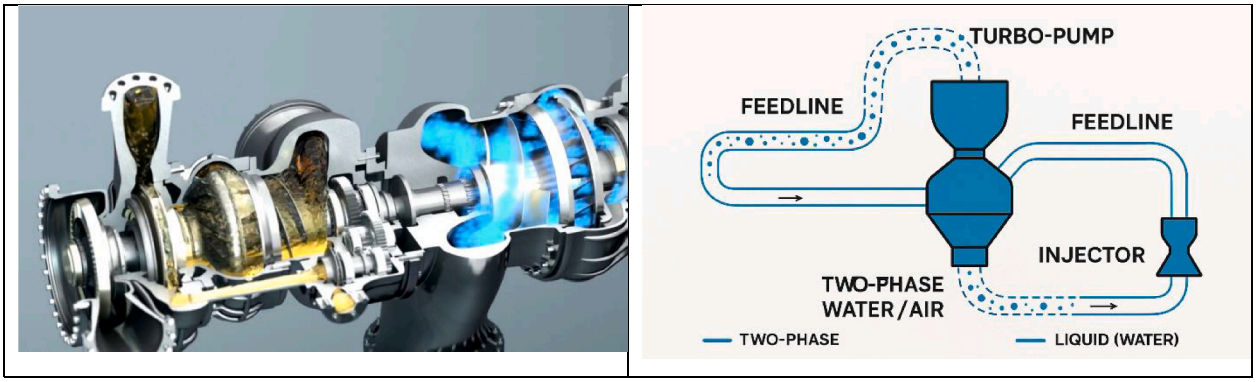

a) Rocket engine Turbopump feedlines in real b) Schematic view of the rocket engine Turbopump feedlines

Fig. 1. Rocket engine Turbopump feedlines schematic view in real and modeling [5,6].

as the two phases pass through certain regions. Consequently, the pressure fluctuation reaches its peak under these specific flow patterns.

Currently, there is a greater emphasis on studying the vibration of fluid-conveying pipes in single-phase flow, while research on pipes carrying gas-liquid two-phase flow is rather limited. Furthermore, during the transportation of a gas-liquid two-phase flow in a pipe, the velocity and pressure of the gas-liquid mixture experience continuous fluctuations, and the distribution of density in the pipe also fluctuates depending on the flow arrangement of the two-phase flow. The dynamic behavior of the pipe not only impacts the dynamic properties of the system of pipes but also affects the flow properties. Ref. [29] used experimental techniques to expand the range of flow rate and void ratio in the air-water circuit. Flexible pipes of different diameters, lengths, and bending stiffness were tested to observe the fluid flexibility of two-phase flow in these pipes. These tests yielded empirical evidence that substantiates the hypothesis of two-phase flow unstable.

Ref. [30] performed a study that specifically examined the mechanism and features of vibration in pipes used for transporting a mixture of gas and liquid. The study focused on the pipeline vibrations theory of single-phase flow, specifically examining the distinct properties exhibited by gas-liquid two-phase flow in various flow patterns. The experimental findings given by Cargnelutti et al. [31] illustrate that models employed to forecast the magnitude of gas-liquid two-phase interaction must take into account parameters such as fluid gravity, tension on the surface, and viscous force. In their study, Miwa et al. [32] found that increasing restrictions can raise the natural frequency of the pipe system in slug flow, which is the flow pattern that has the greatest impact on pipes. This prevents the frequency of the pipe system from being near that of gas-liquid two-phase interaction. An et al. [23] employed a generalized integral transform technique (GITT) to conduct analytical and numerical studies on the dynamic properties of gas-liquid two-phase flow pipes. By verifying the correctness of GITT, the analysis demonstrated that when liquid velocity crosses a critical threshold, the dynamical framework becomes unstable and undergoes divergence.

The magnitude of vibration increases with increased gas volumetric proportion and liquid velocity. Ebrahimi-Mamaghani et al. [33] examined the dynamic characteristics of a vertical pipe transporting a two-phase flow of gas and liquid. The Galerkin discretization method and the eigenvalue analysis approach were utilized to solve the model equations. In addition, they examined the impact of parameters such as weight, flow velocity, structural damping, and gravity on the system's motion, critical flutter velocity, and resonance. Li et al. [30] created a dynamical model for pipes that carry gas-liquid two-phase flow, which includes the inclusion of damping variables. The factors were classified into architectural damping and two-phase flow damping inside the system. In addition, they suggested a correlation for the damping value of the two-phase flow. The study examined the pipe's internal damping reaction to the pipe system's dynamic behavior under various flow patterns. Chehreghani et al. [34] employed an experimental technique to examine the dynamic behavior of suspended pipes. Ma et al. [35], in their studies, utilized the technique of harmonic differential quadrature methodology and experimental testing to examine the vibration of fluid-conveying pipes. Ma et al. [36] recently examined the behavior of a vertical cantilevered pipe subjected to numerous lumped masses caused by internal flow.

Machine learning (ML) algorithms are transforming the field of composite materials by enabling efficient prediction of properties and behaviors without extensive experimental testing [37]. They assist in optimizing material compositions and structures to achieve desired mechanical, thermal, and electrical properties [38]. Also, evaluating the elastic and elastoplastic properties of materials is crucial for understanding their deformation behavior under different loading conditions, enabling accurate predictions of performance and failure [39]. Current research on the interface of ceramic-metal laminated composite materials for armor protection focuses on enhancing interfacial bonding, improving energy dissipation mechanisms, and optimizing the microstructural design to achieve superior impact resistance and ballistic performance [40].

Currently, there is a lack of research on the aerodynamic characteristics of composite pipes used for conveying two-phase flow under airflow. This paper presents the first-ever analysis of the nonlinear aerodynamic responses of a composite pipe conveying two-phase flow. The analysis is based on a data-driven solution. The pipe system being showcased is constructed from a triply periodic minimum material that possesses outstanding mechanical characteristics, including high specific strength, specific stiffness, and energy absorption capabilities. The distribution parameter changes based on the two-phase Reynolds number in a pipe, while maintaining a constant void percentage and adjusting the density ratios. The nonlinear aerodynamic reactions of the pipe reinforced by triply periodic minimum material conveying two-phase flow are accurately simulated using the Nonlinear Von-Karman theory and the general order shear deformation theory. Subsequently, a numerical method is employed to solve the nonlinear governing equations, assisted by nonlinear boundary equations. Once the dataset is acquired through the mathematical modeling portion, a data-driven solution is employed to accurately test, train, and validate the outcomes for reproducing the existing applicable structure in additional intricate scenarios. The suggested data-driven method offers useful insights into the nonlinear aerodynamic responses of reinforced pipes, enabling the design and optimization of sturdy and efficient piping systems for different engineering applications. The novelties of this work can be separated at least into four fields:

1- Modeling a composite pipeline conveying two-phase flow using nonlinear mathematical simulation. 2- Introducing triply periodic minimum material with exceptional mechanical properties for the presented structure. 3- Presenting various functions of the two-phase Reynolds number in a pipeline system. 4- Introducing a data-driven solution with low computational cost to estimate the aerodynamic features of the current system.

2. Basic equations

A flowchart of the presented mathematics simulation (Sections 2 and 3) with more detail is given in Fig. 2.

Fig. 3 depicts a multilayer fiber-reinforced composite pipe with certain dimensions: length (L), outer radius (R_o), inner radius (R_i), and mass per unit length (m_p). The liquid-gas two-phase flow is propelled through the pipe at a velocity denoted as V_f. V_∞ indicate flight speed. The borders of the pipe are fixed, and it is supported by a nonlinear elastic foundation. The coordinate system is positioned in the midplane of the pipe, which is the point where the two-phase flow enters. The x-coordinate represents the position along the length of the pipe, whereas the z-coordinate represents the position perpendicular to the pipe. In this figure, the pressure drop on the upper pipe surface results from supersonic aerodynamic loading.

2.1. Mechanical formulations of FG-TPMS materials

This research focuses on analyzing three distinct models of functionally graded triply periodic minimal surface (FG-TPMS) pipes: Primitive, Gyroid, and I-graph structures. Furthermore, the investigation includes the wrapped package-graph (IWP) configuration. These TPMS forms define the specific traits associated with sheet-like solid geometries [41].

$$\text{Primitive}: \ \psi = \cos(\chi_1 x) + \cos(\chi_2 \theta) + \cos(\chi_3 z), \tag{1a}$$

$$\text{Gyroid}: \ \psi = \sin(\chi_1 x)\cos(\chi_2 \theta) + \sin(\chi_2 \theta)\cos(\chi_3 z) + \sin(\chi_3 z)\cos(\chi_1 x), \tag{1b}$$

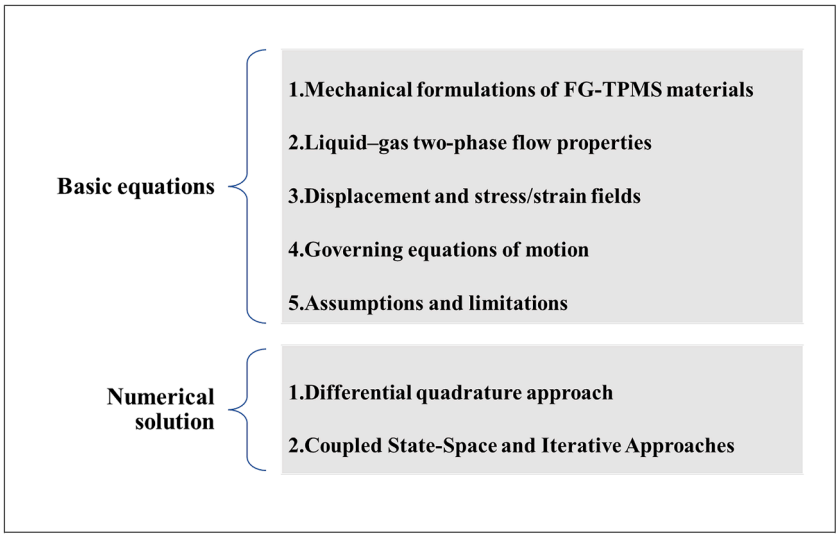

Fig. 2. A flowchart of the presented mathematics simulation (Sections 2 and 3).

$$IWP:\ \psi = 2(\cos(\chi_1 x)\cos(\chi_2\theta)+\cos(\chi_2\theta)\cos(\chi_3 z)+\cos(\chi_3 z)\cos(\chi_1 x)) - (\cos(2\chi_1 x)+\cos(2\chi_2\theta)+\cos(2\chi_3 z)). \tag{1c}$$

The function $\psi(x,\theta,z)$ defines a surface evaluated at a fixed constant, exhibiting a topology characteristic of minimal surfaces.

$$\chi_i = \frac{2\pi n_i}{l_i}, i = 1,2,3. \tag{2}$$

Here, n_i denotes the quantity of unit cells, while l_i signifies their corresponding lengths. This study adopts the curve-fitting approach proposed by Nguyen-Xuan et al. [42], where the volume ratio is characterized using the following expression.

$$V = \frac{V^{TPMS}}{V^m}, \tag{3}$$

V^{TPMS} denotes the overall volume occupied by the TPMS cells, whereas V^m signifies the total volume of the base material. The volume ratio function expressed in Equation (3) can be reformulated as follows:

$$V = \begin{cases} (V_{\max}-V_{\min})V_z^{PatternI}+V_{\min} & \text{Type PA} \\ (V_{\max}-V_{\min})V_z^{PatternII}+V_{\min} & \text{Type PB} \end{cases}, \tag{4}$$

where $V_z^{\text{Type PA}} = \left(\frac{z}{h}+\frac{1}{2}\right)^n$ and $V_z^{\text{Type PB}} = \left(1-\cos\left(\frac{\pi z}{h}\right)\right)^n$.

According to Eq. (4), differentiating between Type *PA* and Type *PB* requires treating them as distinct functions, dependent on the pipe's thickness. Variations in the parameters z and n result in corresponding changes in the volume V_z. Although the two configurations are assigned different values, the discrepancies between them are generally minimal.

2.2. Liquid–gas two-phase flow properties

In this work, the gas void fraction is defined as the proportion of the area taken up by gas (A_G) relative to the inner cross-sectional area of the functionally graded (FG) pipe (A_P) [29].

$$\epsilon_G = \frac{A_G}{A_P} = \frac{A_G}{A_L+A_G}, \tag{5}$$

The variable A_L represents the area that is taken up by the liquid. A_G can be expressed as ϵ_G multiplied by A_P, while A_L can be expressed as $(1-\epsilon_G)$ multiplied by A_P. The drift velocity in a pipe conveying two-phase flow can be expressed using the drift-flux model as follows [43]:

$$V_{GM} = 0.45 M_2 M_3 \sqrt{\frac{gD_h(\rho_L-\rho_G)(1-\epsilon_G)}{\rho_L}}, \tag{6}$$

The parameters in the equation are described as follows: g denotes gravitational acceleration, and D_h is the hydraulic diameter of the pipe, calculated as four times the inner cross-sectional area divided by the wetted perimeter, expressed as $4A_P/(2\pi R_i)$). The symbols ρ_G and ρ_L refer to the mass densities of the gas and liquid phases, respectively.

The drift-flux model (Eq. 6) accounts for relative velocity differences between phases, ensuring realistic simulations of industrial scenarios where phase separation and momentum exchange occur. Future extensions could explore cryogenic or supercritical fluids for aerospace applications, but the current model is validated for conventional two-phase flows. The parameters M_2 and M_3 can be defined as:

$$M_2 = \begin{cases} \left(\frac{0.434}{\log_{10}(\mu_L/0.001)}\right)^{0.15} & \text{if } (\mu_L/0.001) > 10 \\ 1 \text{ if } (\mu_L/0.001) \le 10 \end{cases}, \tag{7a}$$

$$M_3 = \begin{cases} (La/0.025)^{0.9} & \text{if } La < 0.025 \\ 1 \text{ if } La \ge 0.025 \end{cases}. \tag{7b}$$

in which μ_l is the liquid viscosity and $La = \frac{1}{D_h}\sqrt{\frac{\sigma}{g(\rho_L-\rho_G)}}$ (σ is the surface tension). It is important to mention that Eq. (6) is applicable only to horizontal pipes that carry a flow of liquid and gas in two phases. For more information, refer to Ref. [43]. This equation is accurate for Reynolds numbers (Re_{tp}) of the mixed flow ranging from 10 to 5 $\times 10^6$. Figure 4 depicts the relationship between the distribution parameter and the two-phase Reynolds number.

Now it is appropriate to express the gas velocity of the two-phase flow as

$$V_G = C_0 V_f + V_{GM}, \tag{8}$$

The distribution parameter, denoted as C_0, is applicable to horizontal pipes [43]

$$C_0 = \frac{2-(\rho_G/\rho_L)^2}{1+\left(Re_{tp}/1000\right)^2} + \frac{\left[\left(\sqrt{\left(1+(\rho_G/\rho_L)^2\right)/2}\right)^{(1-\epsilon_G)}\right]^{2/5}}{1+\left(1000/Re_{tp}\right)^2}, \tag{9}$$

In which

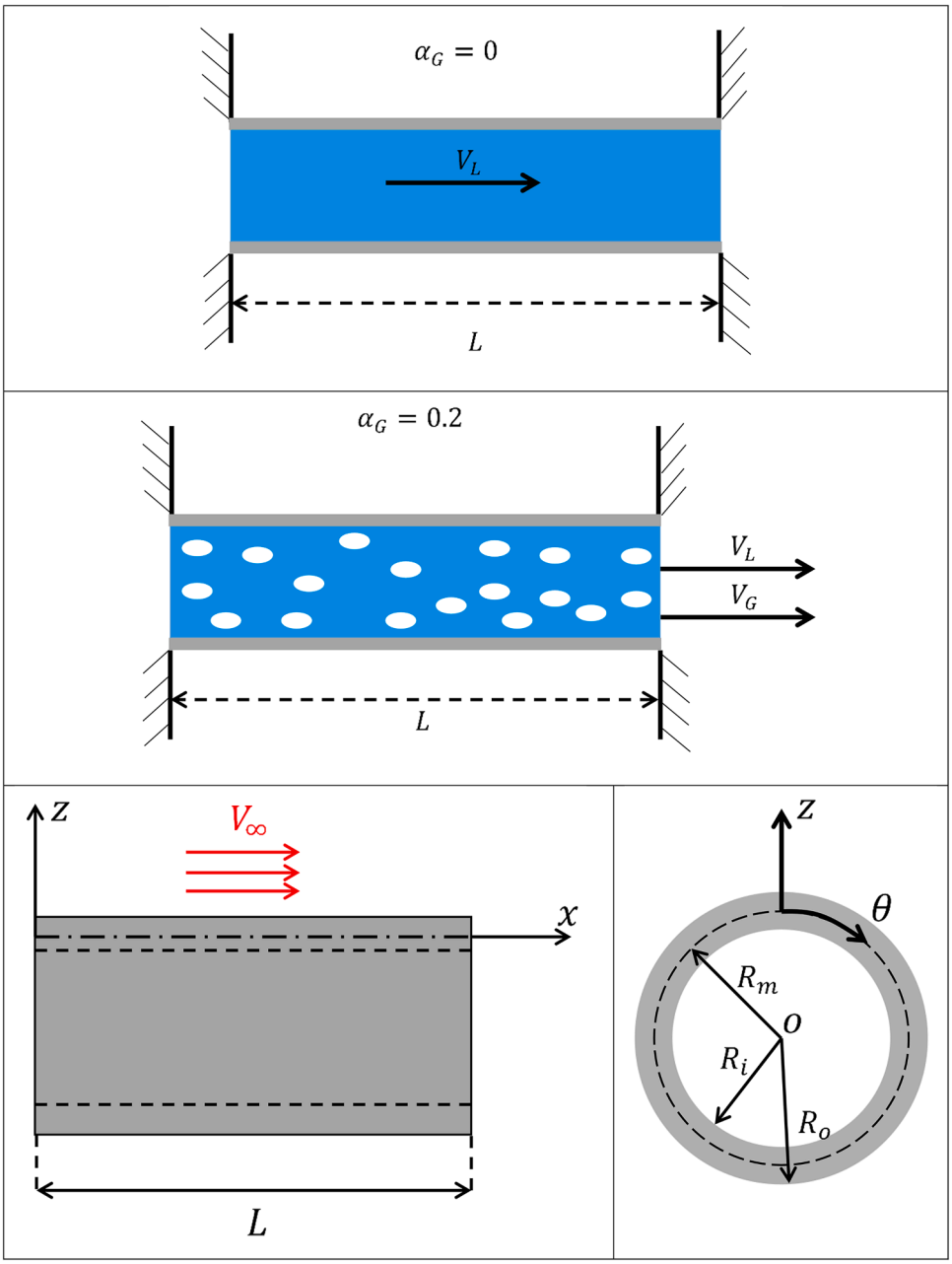

Fig. 3. A schematic view of the FG-TPMS reinforced pipe conveying two-phase flow under airflow.

$$Re_{tp} = \frac{V_f \rho_L D_h}{\mu_L}. \tag{10}$$

To determine the velocity of the liquid phase, we utilize the following correlation [44].

$$V_L = V_f - \frac{\epsilon_G V_{GM}}{1-\epsilon_G}. \tag{11}$$

It is important to note that by determining the values of liquid and gas properties in a two-phase flow (such as ϵ_G, ρ_L and etc.), one can calculate the drift velocity (V_{GM}) in the pipe. Additionally, by establishing the inner radius of the pipe (R_i) and the velocity of the mixture flow (V_f), it is possible to calculate the velocities of the liquid and gas (V_L and V_G, respectively) for the subsequent numerical analysis. In addition, the water-air flow properties are as follows: $\mu_L = 9.10 \times 10^{-4}$Pa.s, $V_f = 2$m/s, $\sigma = 7.18 \times 10^{-2}$N/m, $\rho_G = 1.19$kg/m^3, and, $\rho_L = 997$kg /m^3.

2.3. Displacement and stress/strain fields

The displacement field specified in the present trigonometric shear deformation theory is given as [33],

$$\begin{aligned} u_x(x,\theta,z,t) &= u_0(x,\theta,t) + z u_1(x,\theta,t) + \frac{z^2}{2!}u_2(x,\theta,t) + \frac{z^3}{3!}u_3(x,\theta,t) + \cdots \\ &\quad + \frac{z^k}{k!}u_k(x,\theta,t) \\ &= \sum_{k=0}^{\infty} \frac{z^k}{k!} u_k(x,\theta,t), \end{aligned} \tag{12a}$$

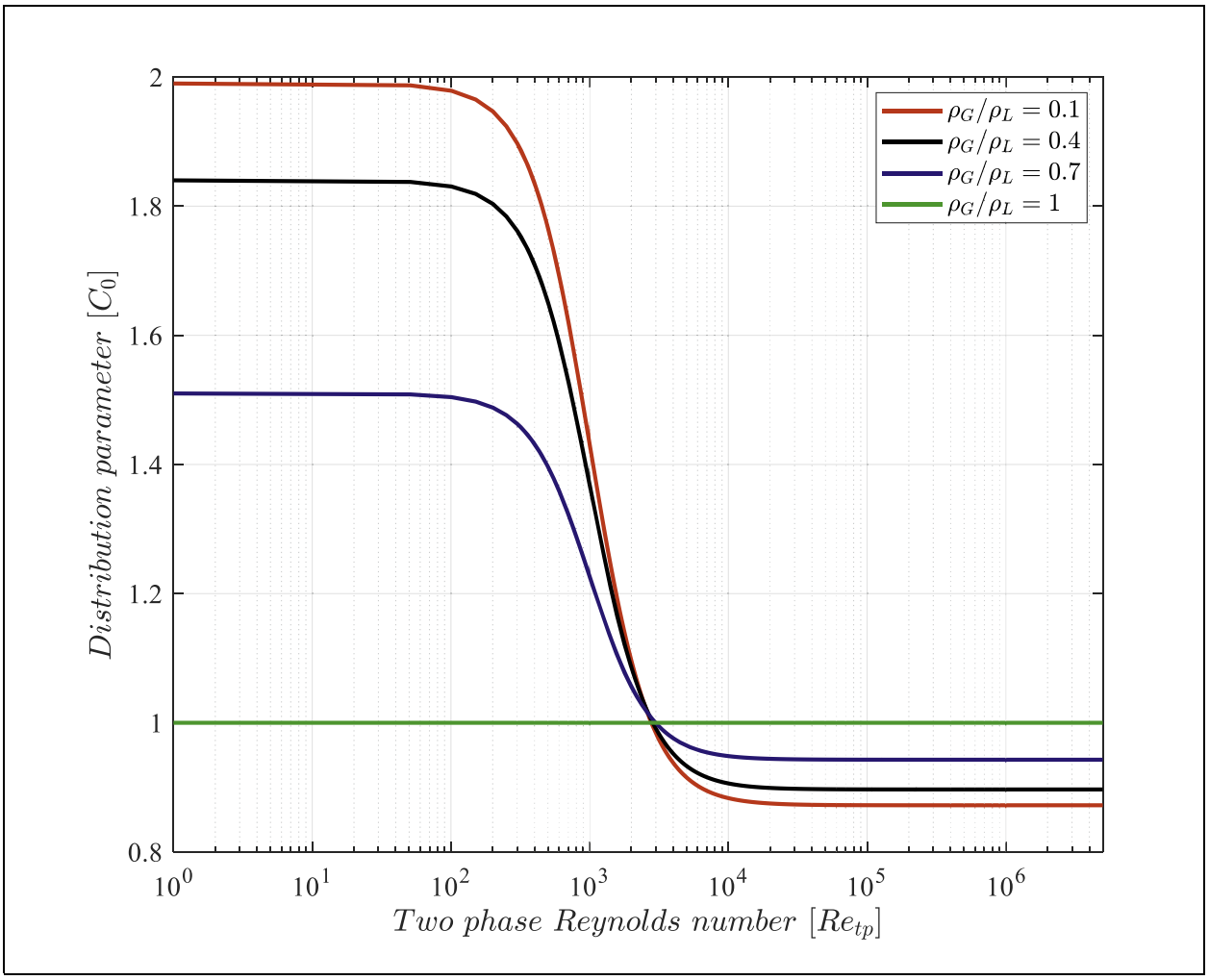

Fig. 4. The distribution parameter varies as a function of the two-phase Reynolds number in a pipe while keeping the void percent constant and modifying the density ratios.

$$u_\theta(x,\theta,z,t) = v_0(x,\theta,t) + zv_1(x,\theta,t) + \frac{z^2}{2!}v_2(x,\theta,t) + \frac{z^3}{3!}v_3(x,\theta,t) + \cdots + \frac{z^k}{k!}v_k(x,\theta,t) = \sum_{k=0}^{\infty}\frac{z^k}{k!}v_k(x,\theta,t), \tag{12b}$$

$$u_z(x,\theta,z,t) = w_0(x,\theta,t) + zw_1(x,\theta,t) + \frac{z^2}{2!}w_2(x,\theta,t) + \frac{z^3}{3!}w_3(x,\theta,t) + \cdots + \frac{z^k}{k!}w_k(x,\theta,t) = \sum_{k=0}^{\infty}\frac{z^k}{k!}w_k(x,\theta,t). \tag{12c}$$

The displacement fields of the composite layer in the x, θ, and z directions are represented by u_x, u_θ, and u_z, respectively, in Eq. (12). u_0, v_0, w_0 are parameters connected with the mid-plane displacement. The terms $u_{1,\ldots,k}$, $v_{1,\ldots,k}$, and $w_{1,\ldots,k}$ represent higher-order terms in the Taylor series expansion. The equation that represents strain displacement in the Von-Karman nonlinear theory is as follows: [45].

$$\varepsilon_{xx} = \frac{\partial u_x}{\partial x} + \frac{1}{2}\left(\frac{\partial u_z}{\partial x}\right)^2,\ \varepsilon_{\theta\theta} = \frac{1}{R}\left(\frac{\partial u_\theta}{\partial \theta} + u_z\right) + \frac{1}{2R^2}\left(\frac{\partial u_z}{\partial \theta}\right)^2,\ \varepsilon_{zz} = \frac{\partial u_z}{\partial z}, \tag{13a}$$

$$\gamma_{x\theta} = \frac{\partial u_\theta}{\partial x} + \frac{1}{R}\frac{\partial u_x}{\partial \theta} + \frac{1}{R}\frac{\partial u_z}{\partial x}\frac{\partial u_z}{\partial \theta},\ \gamma_{\theta z} = \frac{\partial u_\theta}{\partial z} + \frac{1}{R}\frac{\partial u_z}{\partial \theta},\ \gamma_{xz} = \frac{\partial u_x}{\partial z} + \frac{\partial u_z}{\partial x}. \tag{13b}$$

Therefore, the strain components that are not equal to zero are:

$$\varepsilon_{xx} = \frac{\partial u_0}{\partial x} + \cdots + \frac{z^k}{k!}\frac{\partial u_k}{\partial x} + \frac{1}{2}\left(\frac{\partial w_0}{\partial x}\right)^2, \tag{14a}$$

$$\varepsilon_{\theta\theta} = \frac{1}{R}\left(\left(\frac{\partial v_0}{\partial \theta} + \cdots + \frac{z^k}{k!}\frac{\partial v_k}{\partial \theta}\right) + \left(w_0 + \cdots + \frac{z^k}{k!}w_k\right)\right) + \frac{1}{2R^2}\left(\frac{\partial w_0}{\partial \theta}\right)^2, \tag{14b}$$

$$\varepsilon_{zz} = w_1 + \cdots + \frac{z^{k-1}}{(k-1)!}w_k, \tag{14c}$$

$$\gamma_{x\theta} = \left(\frac{\partial v_0}{\partial x} + \cdots + \frac{z^k}{k!}\frac{\partial v_k}{\partial x}\right) + \frac{1}{R}\left(\frac{\partial u_0}{\partial \theta} + \cdots + \frac{z^k}{k!}\frac{\partial u_k}{\partial \theta}\right) + \frac{1}{R}\frac{\partial w_0}{\partial x}\frac{\partial w_0}{\partial \theta}, \tag{14d}$$

$$\gamma_{\theta z} = \left(v_1 + \cdots + \frac{z^{k-1}}{(k-1)!}v_k\right) + \frac{1}{R}\left(\frac{\partial w_0}{\partial \theta} + \cdots + \frac{z^k}{k!}\frac{\partial w_k}{\partial \theta}\right), \tag{14e}$$

$$\gamma_{xz} = \left(u_1 + \cdots + \frac{z^{k-1}}{(k-1)!}u_k\right) + \left(\frac{\partial w_0}{\partial x} + \cdots + \frac{z^k}{k!}\frac{\partial w_k}{\partial x}\right). \tag{14f}$$

The constitutive equation for linear elastic solids describes the mathematical relationship between stress and strain.

$$\sigma_{xx} = \left\{\frac{\nu^{TPMS}E^{TPMS}}{(1+\nu^{TPMS})(1-2\nu^{TPMS})}\right\}\varepsilon_{xx} + \left\{\frac{(1-\nu^{TPMS})E^{TPMS}}{(1+\nu^{TPMS})(1-2\nu^{TPMS})}\right\}\varepsilon_{\theta\theta} + \left\{\frac{(1-\nu^{TPMS})E^{TPMS}}{(1+\nu^{TPMS})(1-2\nu^{TPMS})}\right\}\varepsilon_{zz}, \tag{15a}$$

$$\sigma_{\theta\theta} = \left\{\frac{(1-\nu^{TPMS})E^{TPMS}}{(1+\nu^{TPMS})(1-2\nu^{TPMS})}\right\}\varepsilon_{xx} + \left\{\frac{\nu^{TPMS}E^{TPMS}}{(1+\nu^{TPMS})(1-2\nu^{TPMS})}\right\}\varepsilon_{\theta\theta} + \left\{\frac{(1-\nu^{TPMS})E^{TPMS}}{(1+\nu^{TPMS})(1-2\nu^{TPMS})}\right\}\varepsilon_{zz}, \tag{15b}$$

$$\sigma_{zz} = \left\{\frac{(1-\nu^{TPMS})E^{TPMS}}{(1+\nu^{TPMS})(1-2\nu^{TPMS})}\right\}\varepsilon_{xx} + \left\{\frac{(1-\nu^{TPMS})E^{TPMS}}{(1+\nu^{TPMS})(1-2\nu^{TPMS})}\right\}\varepsilon_{\theta\theta} + \left\{\frac{\nu^{TPMS}E^{TPMS}}{(1+\nu^{TPMS})(1-2\nu^{TPMS})}\right\}\varepsilon_{zz}, \tag{15c}$$

$$\tau_{\theta z} = G^{TPMS}\gamma_{\theta z},\ \tau_{xz} = G^{TPMS}\gamma_{xz},\ \tau_{x\theta} = G^{TPMS}\gamma_{x\theta}. \tag{15d}$$

E^{TPMS}, G^{TPMS} and ν^{TPMS} denote the Young's modulus, shear modulus, and Poisson's ratio of FG-TPMS materials, respectively. As per the established data model [42], these values are computed and shown in Table 1.

This section presents numerical case studies for various FG-TPMS pipe configurations. Six distinct volume distribution patterns are explored, each maintaining an average volume fraction ($V_{average}$) of 0.35, as specified by Eq. (4). These scenarios are detailed in Table 2. To perform the necessary integration within the framework of the mesh-free method, three-node triangular elements are utilized, with each element incorporating a 3 × 3 integration scheme. The fundamental material properties are as follows: Young's modulus (E^m) is 200 GPa, density (ρ^m) is 8000 kg/m^3, and Poisson's ratio (ν^m) is 0.3.

2.4. Governing equations of motion

Hamilton's principle [46–48] establishes all fundamental relationships, encompassing both boundary conditions and governing equations.

Table 1
Mechanical properties of FG-TPMS materials.

TPMS	Mechanical properties	V
Primitive	$E^{TPMS} = E^m\{\begin{matrix}0.317V^{1.264}\\1.007V^{2.006}-0.007\end{matrix}$	$\begin{matrix}V\le 0.25\\V>0.25\end{matrix}$
	$G^{TPMS} = G^m\{\begin{matrix}0.705V^{1.189}\\0.953V^{1.715}+0.047\end{matrix}$	$\begin{matrix}V\le 0.25\\V>0.25\end{matrix}$
	$\nu^{TPMS} = \{\begin{matrix}0.314e^{-1.004V}+0.119\\0.152V^2-0.235V+0.383\end{matrix}$	$\begin{matrix}V\le 0.55\\V>0.55\end{matrix}$
Gyroid	$E^{TPMS} = E^m\{\begin{matrix}0.596V^{1.467}\\0.962V^{2.351}+0.038\end{matrix}$	$\begin{matrix}V\le 0.45\\V>0.45\end{matrix}$
	$G^{TPMS} = G^m\{\begin{matrix}0.777V^{1.544}\\0.973V^{1.982}+0.027\end{matrix}$	$\begin{matrix}V\le 0.45\\V>0.45\end{matrix}$
	$\nu^{TPMS} = \{\begin{matrix}0.192e^{-1.349V}+0.202\\0.402V^2-0.603V+0.501\end{matrix}$	$\begin{matrix}V\le 0.50\\V>0.50\end{matrix}$
IWP	$E^{TPMS} = E^m\{\begin{matrix}0.597V^{1.225}\\0.987V^{1.782}+0.013\end{matrix}$	$\begin{matrix}V\le 0.35\\V>0.35\end{matrix}$
	$G^{TPMS} = G^m\{\begin{matrix}0.529V^{1.287}\\0.960V^{2.188}+0.040\end{matrix}$	$\begin{matrix}V\le 0.35\\V>0.35\end{matrix}$
	$\nu^{TPMS} = \{\begin{matrix}2.597e^{-0.157V}-2.244\\0.201V^2-0.227V+0.326\end{matrix}$	$\begin{matrix}V\le 0.13\\V>0.13\end{matrix}$

Table 2
Six different volume distribution patterns with $V_{average} = 0.35$ [18].

Parameter	PA1	PA2	PA3	PB1	PB2	PB3
n	1.0	3.0	6.5	0.561	1.757	3.943
V_{min}	0.20	0.20	0.25	0.20	0.20	0.25
V_{max}	0.5	0.8	1.0	0.5	0.8	1.0

$$\int_{t_1}^{t_2}\left(\delta\Pi_{liquid} + \delta\Pi_{gas} + \delta\Pi_{pipe} - (\delta\Pi_e - \delta\Pi_{w_1} - \delta\Pi_{w_2})\right)dt = 0, \tag{16}$$

The velocity vector corresponding to any location on the structure can be determined here:

$$v_{pipe} = \frac{\partial u_x}{\partial t}\rightarrow i + \frac{\partial u_\theta}{\partial t}\rightarrow j + \frac{\partial u_z}{\partial t}\rightarrow k, \tag{17}$$

The velocity vector of a fluid particle, when accounting for all relevant factors, can be expressed as:

$$v_{liquid} = \left(\frac{\partial u_x}{\partial t} + V_L\frac{\partial u_x}{\partial x} + V_L\right)\rightarrow i + \left(\frac{\partial u_\theta}{\partial t} + V_L\frac{\partial u_\theta}{\partial x}\right)\rightarrow j + \left(\frac{\partial u_z}{\partial t} + V_L\frac{\partial u_z}{\partial x}\right)\rightarrow k, \tag{18a}$$

$$v_{gas} = \left(\frac{\partial u_x}{\partial t} + V_G\frac{\partial u_x}{\partial x} + V_G\right)\rightarrow i + \left(\frac{\partial u_\theta}{\partial t} + V_G\frac{\partial u_\theta}{\partial x}\right)\rightarrow j + \left(\frac{\partial u_z}{\partial t} + V_G\frac{\partial u_z}{\partial x}\right)\rightarrow k. \tag{18b}$$

Eqs. (19a), (19b), and (19c) represent the different components of kinetic energy in the system, namely the gas phase, liquid phase, and pipe. In addition, Eq. (19d) gives the potential energy of the system.

$$\Pi_{\text{liquid}} = \frac{1}{2}\int \rho_{\text{L}}\left[\left(\frac{\partial u_x}{\partial t} + \text{V}_{\text{L}}\frac{\partial u_x}{\partial x} + \text{V}_{\text{L}}\right)^2 + \left(\frac{\partial u_\theta}{\partial t} + \text{V}_{\text{L}}\frac{\partial u_\theta}{\partial x}\right)^2 + \left(\frac{\partial u_z}{\partial t} + \text{V}_{\text{L}}\frac{\partial u_z}{\partial x}\right)^2\right]\text{dV}, \tag{19a}$$

$$\Pi_{\text{gas}} = \frac{1}{2}\int \rho_{\text{G}}\left[\left(\frac{\partial u_x}{\partial t} + \text{V}_{\text{G}}\frac{\partial u_x}{\partial x} + \text{V}_{\text{G}}\right)^2 + \left(\frac{\partial u_\theta}{\partial t} + \text{V}_{\text{G}}\frac{\partial u_\theta}{\partial x}\right)^2 + \left(\frac{\partial u_z}{\partial t} + \text{V}_{\text{G}}\frac{\partial u_z}{\partial x}\right)^2\right]\text{dV}, \tag{19b}$$

$$\Pi_{\text{pipe}} = \frac{1}{2}\int \rho_{\text{p}}\left[\left(\frac{\partial u_x}{\partial t}\right)^2 + \left(\frac{\partial u_\theta}{\partial t}\right)^2 + \left(\frac{\partial u_z}{\partial t}\right)^2\right]\text{dV}, \tag{19c}$$

$$\Pi_{\text{e}} = \int\{\sigma_{\text{xx}}\varepsilon_{\text{xx}} + \sigma_{\theta\theta}\varepsilon_{\text{yy}} + \sigma_{\text{zz}}\varepsilon_{\text{zz}} + \tau_{\text{x}\theta}\gamma_{\text{x}\theta} + \tau_{\theta\text{z}}\gamma_{\theta\text{z}} + \tau_{\text{xz}}\gamma_{\text{xz}}\}\text{dV}. \tag{19d}$$

The following is the mathematical expression for an auxetic foundation [49]:

$$\Pi_{w_1} = \frac{1}{2}\int_A (K_w u_z + D_f\nabla^4 u_z)u_z dA. \tag{20}$$

The Winkler coefficient, Poisson's ratio, and foundation thickness of the auxetic foundation are denoted by the symbols K_w, ν_f, and h_f, respectively. D_f is also equivalent to $\frac{E_f h_f{}^3}{12(1-\nu_f^2)}$; E_f, and ν_f, is taken to be $E_f = 70\ [GPa]$, and $\nu_f = -0.3$ [49]. In this context, the outermost layer on the upper surface of the composite pipe is influenced by subsonic airflow. The aerodynamic pressure acting on this surface contributes to the work done, which is expressed as:

$$\Pi_{w_2} = \int_A \Delta P u_z dA. \tag{21}$$

In this investigation, the pipe is exposed to aerodynamic pressure generated by a supersonic airflow, which is modeled using the linear piston theory. This theory simplifies the aerodynamic interaction by assuming that the pressure at any given point on the surface is solely dependent on its local downwash velocity, without accounting for interactions between neighboring points [50]. It is important to note that the linear piston theory is considered valid only when the free-stream Mach number satisfies $M_\infty > \sqrt{2}$. Based on this theory, the expression for the supersonic aerodynamic pressure load ΔP is given as follows [51]:

$$\Delta P = -\frac{\rho_\infty V_\infty^2}{\sqrt{M_\infty^2 - 1}}\left[\frac{\partial u_z}{\partial x} + \frac{M_\infty^2 - 2}{M_\infty^2 - 1}\frac{1}{V_\infty}\frac{\partial u_z}{\partial t}\right]. \tag{22}$$

Here, ρ_∞, M_∞, and V_∞ represent the local air density, Mach number, and flight velocity, respectively. To simplify the analysis, it is useful to introduce the following dimensionless parameters: the dynamic pressure λ and the mass ratio μ, defined as:

$$\lambda = \frac{\rho_\infty V_\infty^2 L^3}{D_m\sqrt{M_\infty^2 - 1}}, \mu = \frac{\rho_\infty L}{\rho_m h}. \tag{23}$$

where $D_m = \frac{E_m h^3}{12(1-\nu_m^2)}$.

Accordingly, the supersonic aerodynamic pressure can be reformulated in terms of the introduced dimensionless parameters as follows:

$$\Delta P = -\frac{\lambda D_m}{L^3}\frac{\partial u_z}{\partial x} - \sqrt{\frac{\lambda\mu}{\sqrt{M_\infty^2 - 1}}\left(\frac{M_\infty^2 - 2}{M_\infty^2 - 1}\right)^2}\frac{D_m}{\omega_0 L^4}\frac{\partial u_z}{\partial t}, \tag{24}$$

In addition, in the supersonic airflow [50], when $M_\infty \gg 1$, $\frac{M_\infty^2-2}{M_\infty^2-1}\left(\frac{\lambda\mu}{\sqrt{M_\infty^2-1}}\right)^{1/2} \approx \left(\frac{\lambda\mu}{M_\infty}\right)^{1/2}$, then,

$$\Delta P = -\frac{\lambda D_m}{L^3}\frac{\partial u_z}{\partial x} - \sqrt{\frac{\lambda\mu}{M_\infty}}\frac{D_m}{\omega_0 L^4}\frac{\partial u_z}{\partial t}. \tag{25}$$

In this paper, μ/M_∞ is taken to be 0.01 [52].

The motion equations and boundary conditions (In the Appendix) are obtained by substituting Eqs. (19a-d), (20), and (21) into Eq. (16).

2.5. Assumptions and limitations

- Laminar-to-turbulent transition: Re_{tp} range ($10^{-5} \times 10^{6}$) limits applicability to fully turbulent flows.
- Homogeneous void fraction: ϵ_G is assumed constant axially; local variations are neglected.
- Linear aerodynamics: Piston theory (Eq. 22) ignores shock-boundary layer interactions.
- Wall roughness: Neglected in Eq. 6, but accounted for via M_2 (Eq. 7a), which adjusts for liquid viscosity effects.
- Turbulence: Modeled implicitly through Re_{tp} (Eq. 10); explicit k $-\epsilon$ terms are omitted but could be added in future work.
- Flow history: Assumed quasi-steady; flow regime transitions (e.g., bubbly → slug) are treated as instantaneous.

3. Numerical solution

This section outlines the primary phases involved in achieving a numerical solution using the DQA method.

3.1. Differential quadrature approach (DQA)

Using DQA, the p^{th} derivative of $\mathscr{F}(x)$ as a given one-dimensional function would be declared as [53–55]

$$\frac{\partial^p \mathscr{F}(x)}{\partial x^p} = \sum_{j=1}^{N_x} \mathscr{A}_{ij}^{(p)} \mathscr{F}(x_j) \text{for } i = 1, 2, ..., N_x. \tag{26}$$

here $\mathscr{A}_{ij}^{(p)}$ represents the weight coefficients for the ith grid-point ($j = 1, 2, ..., N_x$) and N_x is the total number of grid-points.

According to Eq. (26), $\mathscr{A}_{ij}^{(p)}$ for $i \neq j$ can be derived as:

$$\mathscr{A}_{ij}^{(p)} = p\left(\mathscr{A}_{ii}^{(p-1)}\mathscr{A}_{ij}^{(1)} - \frac{\mathscr{A}_{ij}^{(p-1)}}{x_i - x_j}\right), p = 2, 3, ..., N_x - 1 \text{and } i, j = 1, 2, ..., N_x, \tag{27}$$

here $\mathscr{A}_{ij}^{(1)}$ can be acquired by subsequent equation

$$\mathscr{A}_{ij}^{(1)} = \frac{\mathscr{M}^{(1)}(x_i)}{(x_i - x_j)\mathscr{M}^{(1)}(x_j)}, i, j = 1, 2, ..., N_x \tag{28}$$

Next equation would be employed to determine $\mathscr{A}_{ij}^{(p)}$

$$\mathscr{A}_{ii}^{(p)} = -\sum_{j=1, j\neq i}^{N} \mathscr{A}_{ij}^{(p)}, i = 2, 3, ..., N_x \text{ and } p = 1, 2, ..., N_x - 1, \tag{29}$$

$\mathscr{M}^{(1)}$ in Eq. (28) can be derived as

$$\mathscr{M}^{(1)}(x_k) = -\sum_{j=1, j\neq k}^{N_x} (x_k - x_j), \text{for } k = 1, 2, 3, ..., N_x. \tag{30}$$

3.2. Two-dimensional approximation

The DQA platform allows for the derivation of the first two derivatives of a given two-dimensional function $\mathscr{F}(x, \theta)$ [56]

$$\left.\frac{\partial \mathscr{F}}{\partial x}\right|_{x=x_i,\theta=\theta_j} = \sum_{p=1}^{N_x}\sum_{k=1}^{N_\theta} \mathscr{A}_{ip}^x I_{pk}^\theta \mathscr{F}_{kj}, \tag{31a}$$

$$\left.\frac{\partial \mathscr{F}}{\partial \theta}\right|_{x=x_i,\theta=\theta_j} = \sum_{p=1}^{N_x}\sum_{k=1}^{N_\theta} I_{ip}^x \mathscr{A}_{pk}^\theta \mathscr{F}_{kj}, \tag{31b}$$

$$\frac{\partial}{\partial x}\left(\left.\frac{\partial \mathscr{F}}{\partial \theta}\right|_{x=x_i,\theta=\theta_j}\right) = \sum_{p=1}^{N_x}\sum_{k=1}^{N_\theta} \mathscr{A}_{ip}^x \mathscr{A}_{pk}^\theta \mathscr{F}_{kj}, \tag{31c}$$

$$\left.\frac{\partial^2 \mathscr{F}}{\partial x^2}\right|_{x=x_i,\theta=\theta_j} = \sum_{p=1}^{N_x}\sum_{k=1}^{N_\theta} \mathscr{B}_{ip}^x I_{pk}^\theta \mathscr{F}_{kj}, \tag{31d}$$

$$\left.\frac{\partial^2 \mathscr{F}}{\partial \theta^2}\right|_{x=x_i,\theta=\theta_j} = \sum_{p=1}^{N_x}\sum_{k=1}^{N_\theta} I_{ip}^x \mathscr{B}_{pk}^\theta \mathscr{F}_{kj}. \tag{31e}$$

Here $\mathscr{A}_{pk}^\theta$, $\mathscr{A}_{ip}^x$, $\mathscr{B}_{pk}^\theta$, and $\mathscr{B}_{ip}^x$ are corresponding weight coefficients. Also, N_θ, and N_x shows the number of grid-points considered through the $\theta-$ and $x-$ directions. It must be mentioned that I_{ip}^x, I_{pk}^θ, I_{ip}^x, and I_{pk}^θ represent identity tensors. Polar coordination of the grid-points (x_i, θ_j) can be derived as follows, through the Chebyshev–Gauss–Lobatto function [57]

$$x_i = \frac{L}{2}\left(1 - \cos\left(\frac{(i-1)}{(N_x - 1)}\pi\right)\right) i = 1, 2, 3, ..., N_x, \tag{32a}$$

$$\theta_j = \pi\left(1 - \cos\left(\frac{(j-1)}{(N_\theta - 1)}\pi\right)\right) j = 1, 2, 3, ..., N_\theta. \tag{32b}$$

By substituting Eqs. (31a-e) into governing equations (as mentioned in the appendix section), we have:

$$\mathrm{M}\ddot{\mathrm{d}} + \mathrm{C}\dot{\mathrm{d}} + [\mathrm{K}_L + \mathrm{K}_{NL}]\mathrm{d} = 0. \tag{33}$$

where M, C, K_L, and K_{NL} are mass matrix, damper matrix, linear and nonlinear stiffness matrices, respectively.

d = $\{u_{0ij}{}^T, v_{0ij}{}^T, w_{0ij}{}^T, u_{1ij}{}^T, v_{1ij}{}^T, w_{1ij}{}^T, u_{2ij}{}^T, v_{3ij}{}^T, w_{2ij}{}^T, u_{3ij}{}^T, v_{3ij}{}^T, w_{3ij}{}^T\}^T, (i = j = 1, 2, ..., N_x \times N_\theta)$ is the unknown displacement vector.

Consequently, Eq. (33) can no longer be treated as a standard eigenvalue problem. To address this, the state-space approach is applied as follows:

$$\begin{bmatrix} \mathrm{I} & 0 \\ 0 & \mathrm{M} \end{bmatrix} \begin{Bmatrix} \mathbf{d}_{,t} \\ \mathbf{d}_{,tt} \end{Bmatrix} + \begin{bmatrix} 0 & -\mathrm{I} \\ \mathbf{K}_L + \mathbf{K}_{NL} & \mathrm{C} \end{bmatrix} \begin{Bmatrix} d \\ \mathbf{d}_{,t} \end{Bmatrix} = \begin{Bmatrix} 0 \\ 0 \end{Bmatrix}. \tag{34}$$

where I is the identity matrix of the same dimensions as the other matrices in this problem. By performing a variable transformation defined as $\mathrm{X} = \{\mathbf{d}\ \mathbf{d}_{,t}\}^{\mathrm{T}}$ (here, superscript T denotes the transpose of the vector), Eq. (34) may be simplified as follows:

$$\mathrm{X}_{,t} + \widehat{\mathrm{K}}\mathrm{X} = 0. \tag{35}$$

where

$$\widehat{\mathrm{K}} = \begin{bmatrix} 0 & -\mathrm{I} \\ \mathrm{M}^{-1}(\mathbf{K}_L + \mathbf{K}_{NL}) & \mathrm{M}^{-1}\mathrm{C} \end{bmatrix}. \tag{36}$$

By selecting a harmonic response for the displacement vector transitioned into the state-space as $\mathrm{X} = \mathrm{X}_0 e^{\Omega t}$, the above equation can be expressed in the following eigenvalue style:

$$\mathrm{I}\Omega + \widehat{\mathrm{K}} = 0. \tag{37}$$

Frequency may be evaluated by the Eq. (37) in accordance with an iterative process [58]. The eigenvalue takes the form of a complex number $\Omega = \Omega_R + i\Omega_I$, where the imaginary part represents the frequency of vibrations and the real part denotes the damping parameter for the structure under consideration.

A) Pipeline Block

- Inputs: Material properties (Table 1), displacements (Eqs. 12–14).
- Solver: DQA (Eqs. 26–32) discretizes PDEs; Coupled State-Space and Iterative Approaches are employed for temporal integration.
- Output: Natural frequency.

B) Data Exchange

- Coupling: Fluid velocities (V_L, V_G) update inertial terms in Eqs. (A1–12) (In Appendix).
- Convergence: Iterate until $||d_{ts} - d_{ts-1}|| < 10^{-6}$.

C) Stopping Criterion

- Residual norm $< 10^{-6}$ or maximum iterations (1000).

This modular approach ensures strong coupling while maintaining numerical stability.

4. Introduction to data-driven solution

Hybrid DNN is indeed a data-driven solution. In the context of structural dynamics, hybrid DNNs leverage large datasets containing information on various aspects of the system, such as geometry, material properties, loading conditions, and corresponding responses or behaviors. These datasets are used to train the DNN model, enabling it to learn complex relationships between input parameters and system responses. The term "data-driven" refers to the fact that hybrid DNNs derive their predictive capabilities primarily from the data they are trained on, rather than relying solely on analytical models or theoretical equations. The model learns patterns and relationships present in the data through iterative training processes, adjusting its internal parameters to minimize the difference between predicted and actual responses. By effectively capturing the underlying patterns in the data, hybrid DNNs can provide accurate predictions for various engineering problems, including estimating frequency of structures such as pipes. This data-driven approach offers several advantages, including the ability to handle nonlinearities, adapt to diverse datasets, and provide rapid predictions once trained. Overall, hybrid DNNs serve as powerful data-driven tools in the field of structural dynamics, enabling engineers and researchers to make informed decisions based on data-driven insights and predictions.

DNNs represent an innovative approach in addressing complex engineering problems, particularly in the realm of structural dynamics. Specifically, they serve as a data-driven solution for estimating frequency of pipes subjected to various loading conditions. The concept of hybrid DNNs entails combining the capabilities of traditional DNN architectures with other computational methods or techniques, such as finite element analysis (FEA) or mathematical modeling, to enhance predictive accuracy and efficiency. In the context of estimating frequency of pipes, hybrid DNNs leverage large datasets containing information on pipe geometry, material properties, loading conditions, and corresponding frequency. These datasets are used to train the DNN model, allowing it to learn complex relationships between input parameters and frequency. The integration of DNNs with traditional numerical methods or analytical models enables the model to capture both the intricacies of the underlying physics and the nuances present in the data. The use of hybrid DNNs offers several advantages. Firstly, they can handle nonlinearities and complex interactions between input parameters more effectively compared to traditional analytical approaches. Secondly, they can adapt to diverse and heterogeneous datasets, making them versatile for various pipe configurations and loading scenarios. Additionally, hybrid DNNs can provide rapid predictions once trained, allowing for quick assessment of pipe frequency under different conditions. Overall, hybrid DNNs present a promising avenue for accurately estimating frequency of pipes, offering improved predictive capabilities and computational efficiency compared to traditional methods. Their integration of data-driven techniques with established engineering principles makes them a valuable tool for engineers and researchers in the field of structural dynamics. The mathematical modeling of a hybrid DNN for estimating frequency of a pipe involves representing the architecture and operations of the network. A flowchart of the presented hybrid DNN for the current problem is presented in Fig. 5.

Here's a generalized formulation of the current hybrid DNN algorithm:

1. Input data representation: Let X represent the input data, which includes various features or parameters related to the pipe system. This input data can consist of geometric properties, material properties, loading conditions, etc.
2. Neural Network Architecture: The hybrid DNN architecture typically consists of multiple layers, including input layer(s), hidden layer(s), and output layer(s). Each layer comprises nodes (neurons) that perform computations.
3. Forward Propagation: The forward propagation process involves computing the output of the neural network given an input X. It can be represented as:

$$Z^{[1]} = W^{[1]}X + b^{[1]}$$

$$A^{[1]} = g(Z^{[1]})$$

$$Z^{[2]} = W^{[2]}A^{[1]} + b^{[2]}$$

$$A^{[2]} = g(Z^{[2]})$$

...

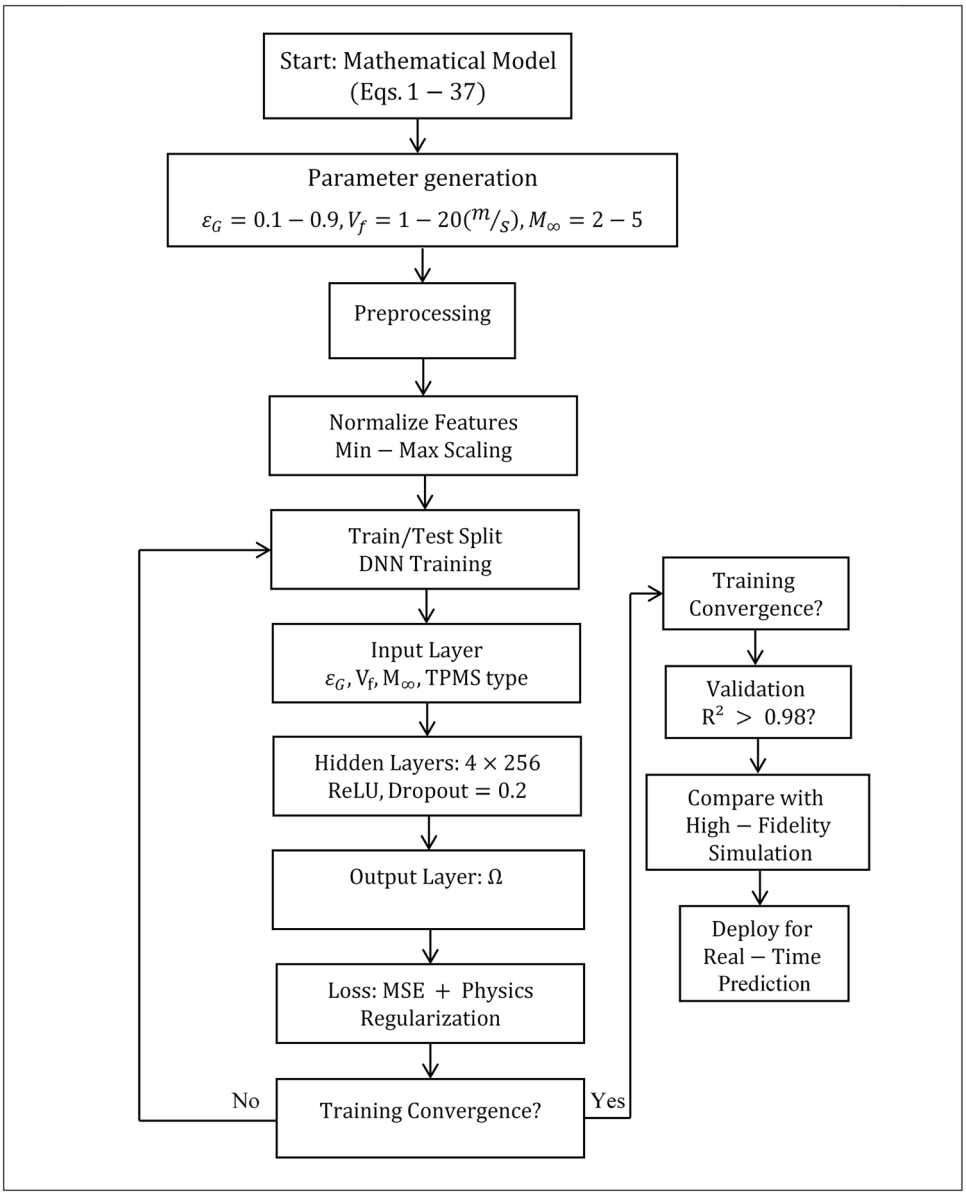

Fig. 5. A flowchart of presented hybrid DNN for the current problem.

$$Z^{[L]} = W^{[L]}A^{[L-1]} + b^{[L]}$$

$$\widehat{Y} = A^{[L]}$$

where:

- $Z^{[1]}$ is the linear activation of layer l.
- $A^{[1]}$ is the output of layer l after applying the activation function g.
- $W^{[l]}$ and $b^{[l]}$ are the weights and biases of layer l, respectively.
- L is the total number of layers in the network.
- $\widehat{Y}$ is the predicted output.

4. Loss function: The loss function measures the difference between the predicted output $\widehat{Y}$ and the actual output Y. It can be defined based on the specific problem being addressed.
5. Backward propagation (gradient descent): The backward propagation process involves computing the gradients of the loss function with respect to the network parameters (weights and biases) and updating these parameters to minimize the loss. This step uses techniques like gradient descent or its variants.
6. Training: The training process iteratively adjusts the network parameters using a dataset of input-output pairs. It involves forward and backward propagation to minimize the loss function.
7. Prediction: Once the network is trained, it can be used to predict frequency for new input data by performing forward propagation.

Overall, the mathematical modeling of a hybrid DNN for estimating frequency of a pipe involves defining the network architecture, specifying activation functions, loss functions, and optimization algorithms, and implementing forward and backward propagation algorithms for training the network. The DNN was trained on a synthetic dataset generated from the mathematical model (Sections 2, and 3) to ensure consistency with the underlying physics. Below are the key details:

1. Data Generation Process

- Input Parameters (Sampled via Latin Hypercube Design):

- Void fraction: $\varepsilon_G \in [0.1, 0.9]$ (10%–90% gas)
- Flow velocity: $V_f \in [1, 20]$ (covering laminar to turbulent regimes)
- Mach number: $M_\infty \in [2, 5]$ (supersonic range)
- TPMS configurations: Primitive, Gyroid, IWP (Table 2) with $V \in [0.2, 1.0]$.
- Pipe geometry: $L/D_h \in [10, 50]$, auxetic foundation stiffness $K_w \in [10^6, 10^9]$ N/m^3.

- Output Variables (Solved via DQA/ Coupled State-Space and Iterative Approaches):
  - Natural frequency: Ω.
- Total Cases: 10,000 simulations (8,000 training + 2,000 testing) with $\Delta t = 0.001$ s, $t_{max} = 1$s.

2. Data Preprocessing

- Normalization: Min-Max scaling applied to inputs (ε_G, V_f,…) and output (Ω).
- Noise Injection: 5% Gaussian noise added to outputs to simulate sensor errors and improve robustness.
- Feature Extraction: Peak frquency (max|Ω|).

3. Validation & Generalization

- Physics-Based Checks:
  - Ensured predictions satisfy drift-flux model (Eq. 6) and energy conservation (Eq. 19d).
  - Penalized violations via loss function regularization.
- Benchmarking:
  - Compared DNN predictions against high-fidelity simulations for unseen cases:
    - Extreme V_f=25m/s (beyond training range).
    - IWP TPMS with V=1.2 (outside Table 2 range).
  - Achieved R^2>0.98 for interpolated cases, R^2>0.92 for extrapolated cases.

4. Limitations

- Flow Regimes: Training data covers bubbly (ε_G<0.3), slug (0.3≤ε_G≤0.7), and annular flows (ε_G>0.7), but churn flow requires additional data.
- Boundary Conditions: Fixed-fixed pipes only; other constraints (e.g., pinned-free) need retraining.

5. Results section

Table 3 summarizes the conditions for the generality of results. This table explicitly defines the range of validity for your two-phase flow model and its structural coupling.

5.1. Validation

Fig. 6 presents a comparative analysis between theoretical predictions and experimental data regarding the dimensionless critical liquid-phase velocity (V_L^{cr}) for a downward cantilevered shell that carries two-phase flow, plotted against the gas void fraction (ε_G). This comparison is conducted in the absence of any tension force acting on the shell. The critical liquid-phase velocity represents the point at which the shell becomes dynamically unstable, a crucial parameter in understanding the behavior of fluid-conveying structures. The red line in the figure represents the theoretical predictions from the present study. The theoretical analysis aims to model the behavior of the two-phase flow within the shell, considering factors such as the flow-induced forces, the structural characteristics of the shell, and the effects of varying gas void fractions. As depicted, the theoretical curve shows a complex relationship between V_L^{cr} and ε_G. Initially, the critical liquid-phase velocity decreases gradually as the gas void fraction increases. This decrease suggests that the introduction of gas into the flow reduces the fluid's ability to stabilize the shell. As ε_G approaches higher values (closer to 1), the curve exhibits a sharp decline in V_L^{cr}, indicating a critical point where the flow becomes significantly destabilized due to the high gas content. The black circles in the figure represent experimental data obtained from Ref. [29]. These data points were collected from physical experiments designed to observe the behavior of the downward cantilevered shell under two-phase flow conditions. The experimental results follow a trend similar to the theoretical predictions, confirming the general validity of the theoretical model. However, some deviations are observed, particularly in the mid-range values of ε_G. These deviations could arise from various sources, including experimental uncertainties, simplifications in the theoretical model, or differences in the physical properties of the materials used in the experiments compared to those assumed in the theoretical analysis. The comparison between the theoretical and experimental data illustrates that while the theoretical model captures the overall trend of the behavior, some discrepancies exist. These differences highlight the complexities involved in accurately predicting the dynamic behavior of structures under two-phase flow conditions. The sharp decline in V_L^{cr} at higher ε_G values is a critical finding, suggesting that beyond a certain gas void fraction, the shell's stability is drastically compromised. This insight is valuable for the design and operation of fluid-conveying structures, particularly in applications where two-phase flow is prevalent. In conclusion, the figure effectively demonstrates the relationship between gas void fraction and the critical liquid-phase velocity, with both theoretical and experimental data contributing to a deeper understanding of the dynamic stability of downward cantilevered shells in two-phase flow systems.

Table 4 compares the natural frequency parameters of stationary isotropic cylindrical shells under S-S boundary conditions, based on experimental and present solutions. The variables considered are the circumferential wave number, the longitudinal wave number, and the corresponding natural frequency values in *Hz*, which are expressed as a

Table 3
Summarizing the conditions for the generality of results.

Parameter	Valid Range	Justification / Limitation	Supporting Citations
Flow Orientation	Horizontal pipes only	Drift-flux model (Eq. 6) assumes negligible gravity-driven stratification. Vertical flows require modified C_0.	[59]
Void Fraction	$0.1 \le \varepsilon_G \le 0.9$	Bubbly (ε_G<0.3) and annular (ε_G>0.7) flows validated experimentally. Slug flow (0.3<ε_G<0.7) has higher uncertainty (±10%).	[60]
Reynolds Number	$10^3 \le Re_{tp} \le 10^6$	Turbulence effects are implicitly captured via M_2, M_3 (Eqs. 7a–b). Laminar (Re_{tp}<10^3) and highly turbulent (Re_{tp}>10^6) regimes need calibration.	[61]
Pipe Diameter	10 mm ≤ D_h ≤ 100 mm	Empirical validation for small-to-medium diameters. Scalability to microchannels (D_h<10 mm) requires wall-shear terms.	[62]
Density Ratio	$100 \le \rho_L/\rho_G \le 1000$	Water-air (ρ_L/ρ_G≈840) is the primary focus. Extrapolation to cryogenic fluids needs V_{GM} recalibration.	[63]
Mach Number	$M_\infty \le 5$	Linear piston theory (Eq. 22) valid for supersonic but not hypersonic flows (M_∞>5).	[50]
TPMS Type	Primitive, Gyroid, IWP	Mechanical properties (Table 1) fitted to V≤1.0. Higher porosity ($V > 1$) requires new curve-fitting.	[64]

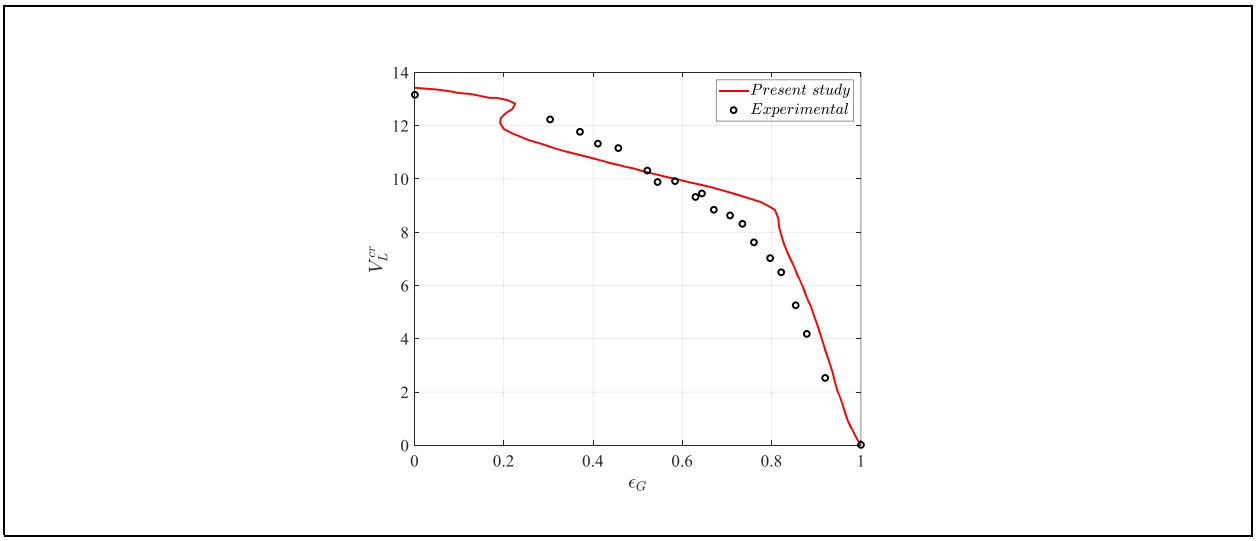

Fig. 6. The dimensionless critical liquid-phase velocity of a downward cantilevered shell carrying two-phase flow is compared between theoretical and experimental data (Ref. [29]) against the gas vacancy percentage in the absence of the tension force.

Table 4
Comparisons of stationary isotropic cylindrical shells' natural frequency parameters/2π (Hz) with S-S boundary conditions.

m	n	Ref. [65]	Experiments [66]	Present solutions
1	7	488.424	484.6	487.3213
	8	494.495	489.6	493.2315
	9	551.750	546.2	550.5621
	6	555.876	553.3	554.6523
	10	642.650	636.8	641.12434
	5	723.524	722.1	722.6722
	11	756.633	750.7	755.8954
	12	888.251	882.2	887.7622
2	10	972.446	968.1	971.3891
	11	988.407	983.4	987.9824

*m: Circumferential wave numbers, n: Longitudinal wave numbers

fraction of $2\pi/Hz$. The comparison spans different reference materials, experiments, and present solutions. From the table, it is observed that the natural frequency values in the "Present solutions" column closely approximate those in the "Experiments" column. These results are specifically calculated for cylindrical shells made from isotropic material with defined geometrical properties, such as length $L = 0.2\ m$, radius $R = 0.1\ m$, and height $h = 0.247$ [10^{-3} m]. For example, for $m = 1$ and $n = 1$, the experimental value is 484.6 Hz, and the present solution is 487.3213 Hz, indicating a small difference in the natural frequency prediction. This consistency between the two approaches suggests the reliability of the mathematical model in predicting the dynamic behavior of isotropic cylindrical shells under the specified conditions. Such comparisons are crucial for validating mathematical models, offering valuable insights for the design of piping systems in engineering applications, particularly those involving composite and isotropic materials.

5.2. Parametric results

Table 5 presents a convergence study for the DQA applied to analyze the nonlinear aerodynamic flutter responses of composite pipes conveying two-phase flow. The study evaluates the dimensionless imaginary part of frequency for varying grid resolutions (N_x, N_θ), ranging from $(5,5)$ to $(15,15)$. The model parameters include a primitive configuration, PA1, $\Omega = 0.4 \times .\omega_{11}$, $\epsilon_G = 0.1$, and $t = 0.5$ [ms]. The results demonstrate convergence as the grid resolution increases. The

Table 5
A convergence study $(\overline{\Omega}_I)$ for the current DQA (PA1, $V_f = 2\ [\frac{m}{s}]$, $\epsilon_G = 0.1$, $K_w = 10^6\ [\frac{N}{m^3}]$, $\nu_f = -0.3$, $h_f = \frac{h}{3}$).

	(N_x, N_θ)					
Model	(5,5)	(7,7)	(9,9)	(11,11)	(13,13)	(15,15)
IWP	0.3943	0.3854	0.3848	**0.3847**	0.3847	0.3847
Gyroid	0.5423	0.5232	0.5329	**0.5228**	0.5228	0.5228
Primitive	0.4218	0.4039	0.4033	**0.4032**	0.4032	0.4032

bolded values highlight the points of convergence, indicating the minimal grid size required for accurate results. This study validates the DQA's reliability for the problem, ensuring grid independence and numerical precision in capturing the nonlinear flutter dynamics of composite pipes under two-phase flow conditions.

Fig. 7 illustrates the nonlinear aerodynamic flutter responses of a pipe conveying two-phase flow, specifically for the PA1 type configuration. The plots compare the behavior of three material models—"Primitive," "Gyroid," and "IWP"—under varying aerodynamic pressure parameter. The real and imaginary parts of the natural frequency are presented as functions of the aerodynamic pressure parameter. The plot shows that as the aerodynamic pressure increases, the imaginary part of the frequency corresponding to the first mode increases significantly for the "Gyroid" model, while it remains more stable for the "Primitive" and "IWP" models. In contrast, the real part of the frequency stays at zero until the critical aerodynamic pressure (flutter point) is reached. Upon crossing this point, the real frequency becomes non-zero, indicating the onset of damping in the system due to increased aerodynamic pressure. The results highlight that each model responds differently to the increase in aerodynamic pressure, with the "Gyroid" model showing the most significant changes in natural frequencies. The right panel shows the second imaginary part of the natural frequency for the same models and parameters. Also, the imaginary frequency increases with λ_∞, but the second frequency demonstrates a different trend, decreasing initially and then stabilizing after a critical aerodynamic pressure. The point where the first and second imaginary frequencies converge marks the onset of flutter, which is vital for ensuring the structural integrity of the pipe system.

Fig. 8 focuses on the nonlinear aerodynamic flutter responses of a pipe conveying two-phase flow for the PB1 type configuration. Similar to Fig. 7, the behavior of three material models— "Primitive," "Gyroid,"

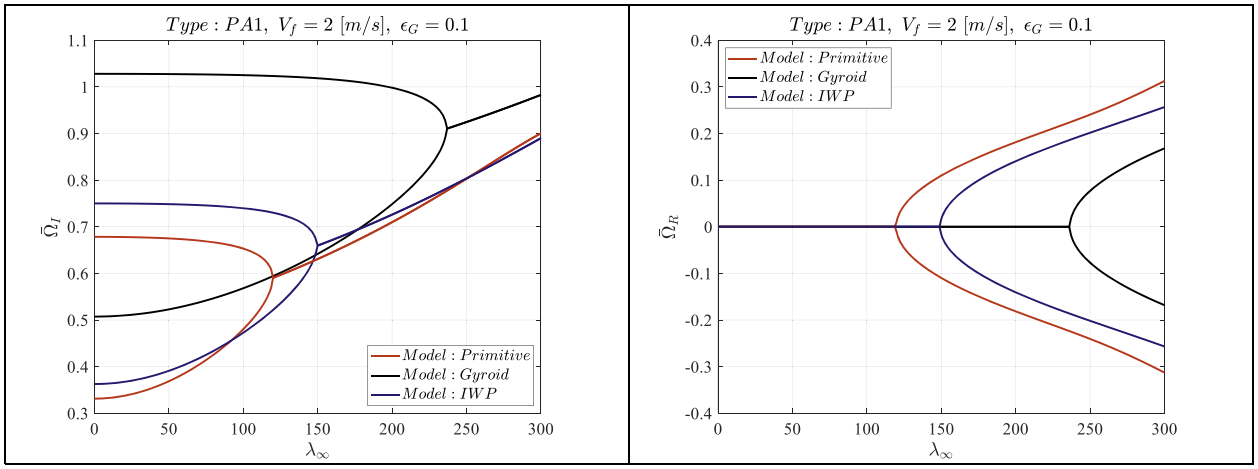

Fig. 7. The nonlinear aerodynamic flutter responses of a pipe conveying two-phase flow, for different models of TPMS considering PA1 type of TPMS.

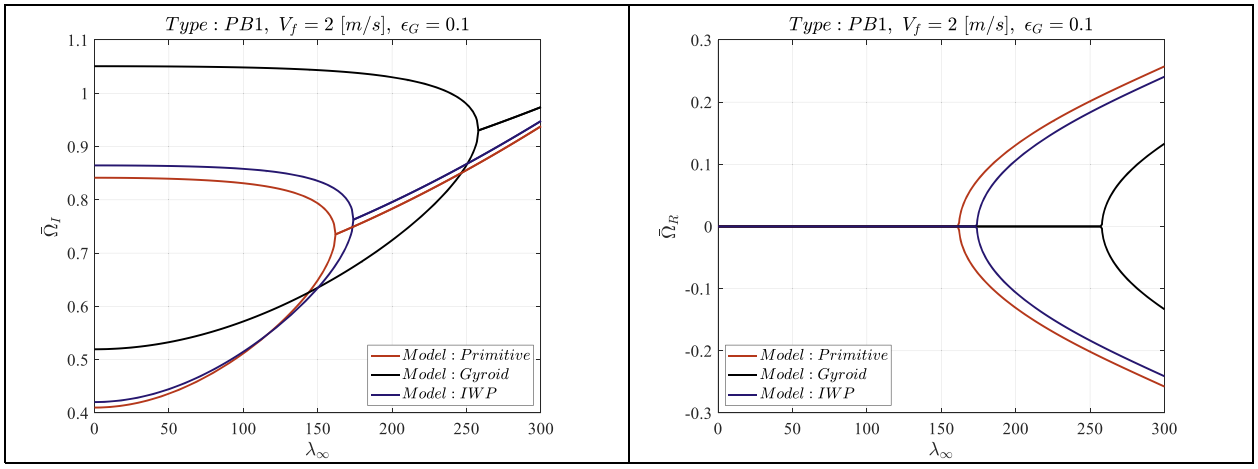

Fig. 8. The nonlinear aerodynamic flutter responses of a pipe conveying two-phase flow, for different models of TPMS considering PB1 type of TPMS.

and "IWP"—is compared under different values of the aerodynamic pressure parameter. The real and imaginary parts of the natural frequency are plotted against the aerodynamic pressure parameter. As λ_∞ increases, the imaginary part of the first natural frequency for the "Gyroid" model shows an upward trend, while for the "Primitive" and "IWP" models, the increase is less pronounced. The real frequency remains at zero until the critical aerodynamic pressure is reached, after which it increases, signifying the damping effect of aerodynamic pressure. The "Gyroid" model exhibits a more substantial change in frequency compared to the other models, reflecting its sensitivity to the aerodynamic pressure parameter. The figure shows the second imaginary part of the natural frequency. Also, the imaginary frequency

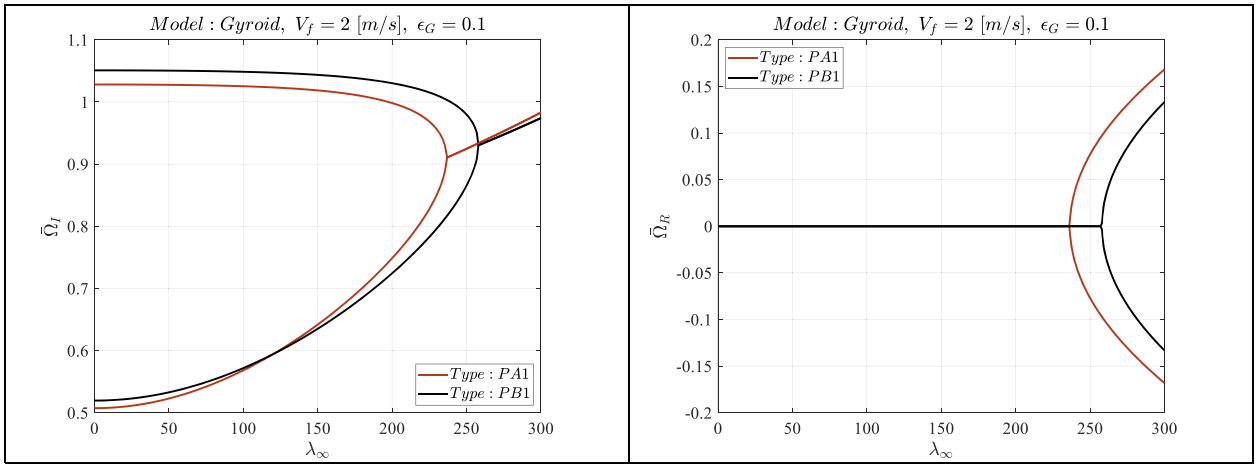

Fig. 9. The nonlinear aerodynamic flutter responses of a pipe conveying two-phase flow, for different types of TPMS considering Gyroid model of TPMS.

increases with the aerodynamic pressure, but the rate of change differs among the models. At the critical aerodynamic pressure, the two imaginary frequencies converge, signaling the onset of flutter. This flutter point is critical for identifying potential instability in the piping system. After crossing the flutter threshold, the real frequency becomes non-zero, indicating that damping occurs as a result of the increased aerodynamic pressure. This figure, like Fig. 7, emphasizes how the material distribution pattern influences the dynamic stability of pipes conveying two-phase flows. Understanding these responses is crucial for the design and optimization of robust piping systems in various engineering fields.

Fig. 9 presents the nonlinear aerodynamic flutter responses of a pipe conveying two-phase flow, utilizing the "Gyroid" model. The figure compares three different types of pipe configurations: PA1, and PB1. The real and imaginary parts of the natural frequency are plotted as functions of the aerodynamic pressure parameter λ_∞ for the PA1, and PB1 types. The results show that for both PA1 and PB1 types, the real part of the frequency remains zero until a critical aerodynamic pressure is reached, after which it becomes non-zero, signaling the onset of damping. The PB1 type shows the most significant shift in the real and imaginary parts of the frequencies as λ_∞ increases, indicating a higher sensitivity to aerodynamic pressure. The PB1 type remains more stable compared to the PA1 type, with less variation in both real and imaginary frequencies. The figure focuses on the second imaginary part of the frequency for the same models. The plot illustrates that as λ_∞ increases, the imaginary frequency increases for the PA1 type, while the PB1 types show more gradual changes. The critical flutter point is marked by the intersection of the two imaginary frequency curves. Beyond this point, damping becomes significant due to the increase in aerodynamic pressure.

Fig. 10 illustrates the effect of the aerodynamic pressure parameter on the natural frequency and damping parameter of frequency for Gyroid-type of TPMS pipes of three configurations: PB1, PB2, and PB3. The system operates at a velocity of $V_f = 2\ m/s$ with a gas void fraction $\epsilon_G = 0.1$. At low aerodynamic pressures, the natural frequency remains nearly constant across all models. As λ_∞ increases, two modes of Ω_I evolve differently and converge at a critical aerodynamic pressure, marking the flutter onset. Beyond this point, the frequency splits, with one branch decreasing rapidly, indicating loss of stability. PB3 maintains higher natural frequencies over a larger pressure range, whereas PB1 exhibits the most rapid decline. At low λ_∞, the damping is positive and stable for all three configurations. As λ_∞ increases, one mode of Ω_R decreases and approaches zero. At the flutter boundary, the damping values of the two modes coincide, signifying neutral stability. Beyond flutter, Ω_R becomes nonzero, showing that aerodynamic forces inject energy into the system, thereby amplifying oscillations. Comparing the TPMS types, PB3 exhibits the most favorable damping behavior, while PB1 shows earlier degradation of stability. Together, the results confirm that Ω_I identifies natural frequency evolution, while Ω_R highlights energy exchange and damping, both essential for predicting flutter onset.

Fig. 11 presents the nonlinear aerodynamic flutter characteristics of a gyroid-type TPMS composite pipe subjected to varying mixture velocities (V_f= 2, 5, and 10 m/s) at a constant gas void fraction ($\epsilon_G = 0.1$). The plots illustrate the evolution of the real part and the imaginary part of the complex frequency as a function of the aerodynamic pressure parameter. In the left subfigure, Ω_I remains close to unity in the low λ_∞ regime, but diverges into two distinct branches as λ_∞ increases. The upper branch grows steadily, while the lower branch diminishes, indicating the progressive influence of aerodynamic loading on frequency splitting. The intersection of these two branches marks the onset of flutter instability, where the system loses aeroelastic stability. The right subfigure shows the corresponding variation in Ω_R, which captures the damping and growth rates of oscillatory modes. Initially, Ω_I is nearly zero, reflecting a stable condition. However, as λ_∞ increases, one branch of Ω_I rises positively while the other declines negatively, highlighting the destabilizing aerodynamic contribution. Notably, higher mixture velocities shift the critical flutter boundary to lower λ_∞ values, meaning that pipes conveying faster two-phase flows are more prone to flutter instability. This figure underscores the direct influence of fluid transport velocity on aeroelastic stability margins in TPMS-reinforced composite pipes. The results provide valuable insights for predicting flutter onset in high-velocity multiphase pipeline systems across nuclear, aerospace, and petrochemical applications.

Fig. 12 illustrates the nonlinear aerodynamic flutter responses of a gyroid-type TPMS composite pipe at a fixed mixture velocity ($V_f = 2$ m/s) for varying gas void fractions ($\epsilon_G = 0.1, 0.3, 0.5$). The left subfigure shows the evolution of the imaginary part of frequency with increasing aerodynamic pressure parameter. At lower λ_∞, Ω_I remains near unity and stable; however, with increasing λ_∞, the frequency branches split, with one increasing and the other decreasing. The critical λ_∞ is identified at the intersection of these two branches, signifying the onset of flutter. Importantly, as ϵ_G increases, this critical boundary occurs at lower λ_∞, indicating that higher void fractions reduce the aeroelastic stability margin. The right subfigure demonstrates the variation of the real part of frequency, representing damping characteristics. At low λ_∞, Ω_R remains close to zero, suggesting stable oscillations. As aerodynamic loading intensifies, Ω_I branches diverge, with one increasing positively and the other decreasing negatively. Larger void fractions accelerate this divergence, amplifying the damping or growth rate and causing earlier instability onset. Physically, this behavior reflects the destabilizing

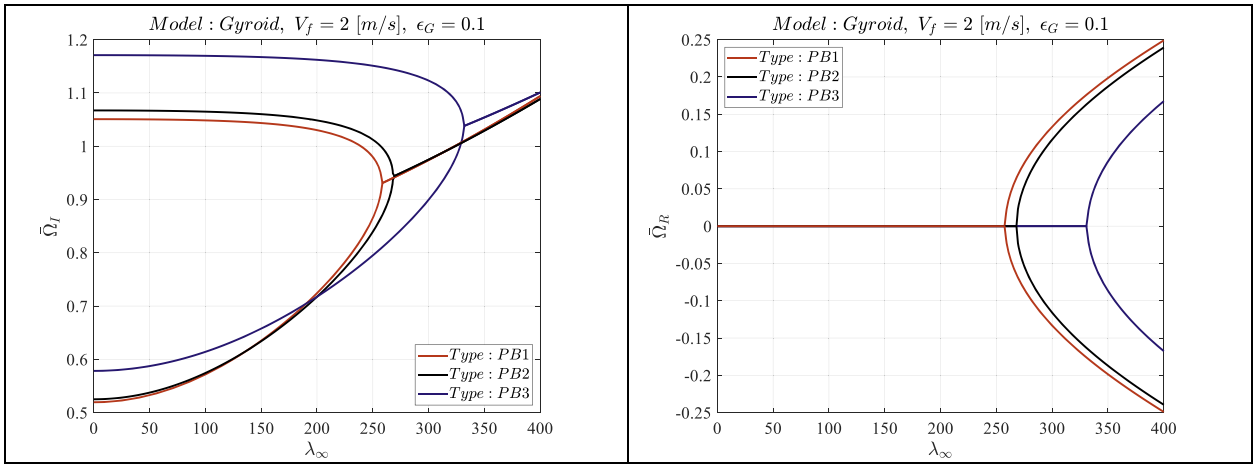

Fig. 10. The effect of the aerodynamic pressure parameter on the natural frequency and damping parameter of frequency for Gyroid-type TPMS pipes of three configurations: PB1, PB2, and PB3.

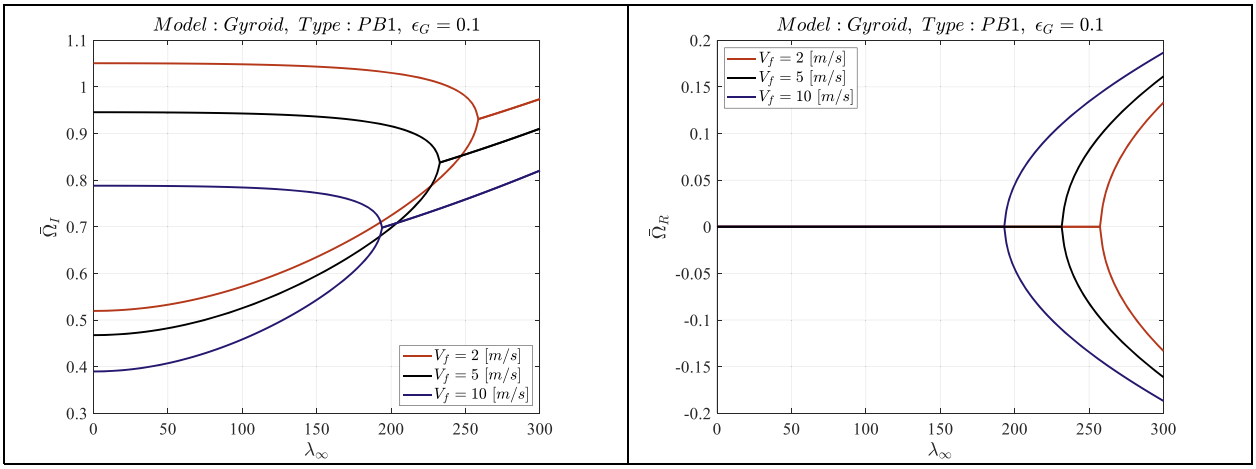

Fig. 11. The nonlinear aerodynamic flutter characteristics of a gyroid-type TPMS composite pipe subjected to varying mixture velocities.

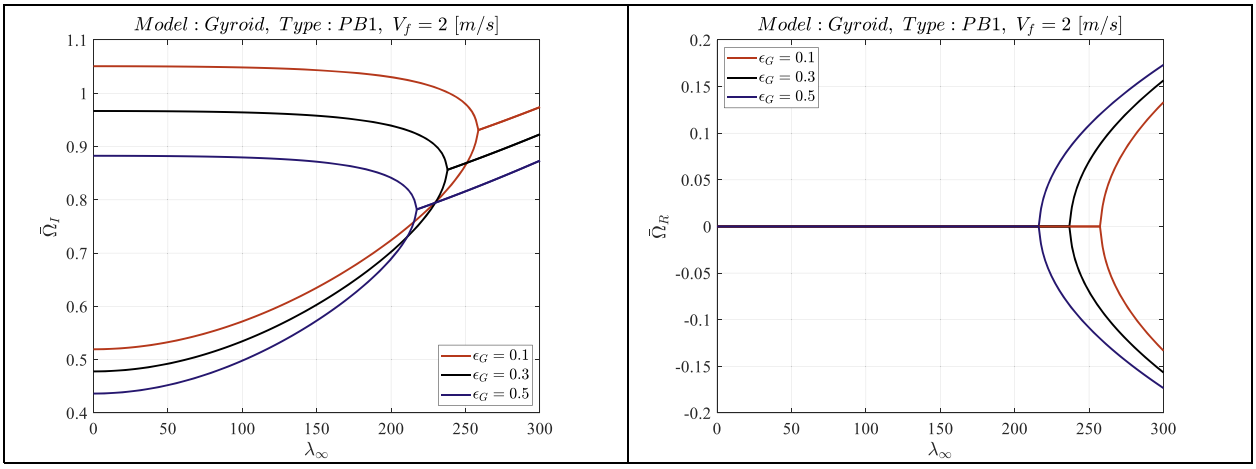

Fig. 12. The nonlinear aerodynamic flutter responses of a gyroid-type TPMS composite pipe at a fixed mixture velocity for varying gas void fractions.

effect of increased gas content in the two-phase mixture, which weakens structural resistance to aeroelastic forces. Overall, the results demonstrate that void fraction plays a decisive role in governing flutter behavior, with higher gas content significantly lowering the stability threshold. This figure highlights the necessity of precise void fraction control in engineering applications involving multiphase fluid transport to ensure reliable operation and avoid premature aeroelastic instabilities.

Fig. 13 depicts the nonlinear aerodynamic flutter response of a gyroid-type TPMS composite pipe at a fixed mixture velocity (V_f= 2 m/

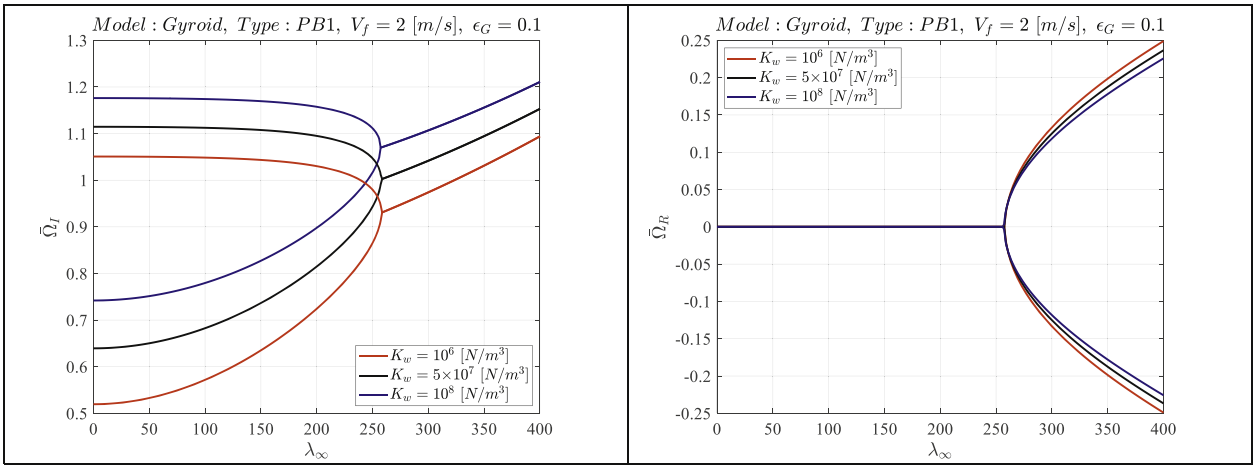

Fig. 13. The nonlinear aerodynamic flutter response of a gyroid-type TPMS composite pipe at a fixed mixture velocity and void fraction with varying Winkler foundation stiffness values.

s) and void fraction (ϵ_G= 0.1), with varying Winkler foundation stiffness values (K_w=10^3, 10^5, and 10^7 N/m^2). The left subfigure illustrates the evolution of the imaginary part of frequency with respect to the aerodynamic pressure parameter. At low λ_∞, Ω_R values remain stable near unity across all K_w values, but as λ_∞ increases, the frequencies split into diverging branches, marking the classical flutter mechanism. Notably, higher foundation stiffness delays the critical flutter point to larger λ_∞ values, thereby improving stability margins. The right subfigure demonstrates the corresponding imaginary frequency component. Initially, Ω_I remains zero, indicating stable oscillations. With increasing λ_∞, Ω_I bifurcates into positive and negative branches. The divergence magnitude decreases with increasing K_w, reflecting a stronger foundation stiffness suppressing instability growth rates. The results confirm that a stiffer foundation provides greater resistance to aeroelastic excitation, effectively postponing the onset of flutter and reducing the amplitude of unstable oscillations. Physically, the auxetic Winkler foundation enhances structural stiffness and damping capacity, reducing susceptibility to destabilizing aerodynamic pressures. These findings highlight the critical role of foundation stiffness in the aeroelastic design of TPMS-reinforced composite pipes conveying two-phase flow. By optimizing K_w, engineers can achieve greater safety and operational reliability in aerospace, nuclear, and petrochemical applications where flutter-induced instability may otherwise compromise system performance.

Fig. 14 presents the influence of pipe elastic foundation thickness ratio on the nonlinear aerodynamic flutter response of a gyroid-type TPMS composite pipe at $V_f = 2\ m/s$ and $\epsilon_G = 0.1$. Three thickness configurations are considered: $h_f = 0,\ h/3$, and $h/2$, where h denotes the total wall thickness. The left subfigure shows the variation of the real frequency component as a function of λ_∞. At low aerodynamic loading, Ω_l remains stable for all thickness ratios, but diverges into two branches as λ_∞ increases. A thicker elastic foundation wall shifts the flutter onset to higher λ_∞ values, signifying improved aeroelastic stability, while thinner elastic foundation walls exhibit earlier bifurcation, indicating vulnerability to flutter at lower aerodynamic pressures. The right subfigure illustrates the corresponding imaginary frequency component. At small λ_∞, Ω_R is zero for all cases, consistent with stable oscillations. As λ_∞ increases, Ω_R branches into positive and negative values, representing growing instability. The rate of divergence is more pronounced for thinner walls, demonstrating a reduced capacity to withstand aerodynamic excitation. In contrast, a thicker elastic foundation maintains reduced divergence, signifying delayed flutter onset and better damping control. These observations emphasize the importance of wall thickness in governing the aeroelastic behavior of composite TPMS pipes. Structurally, thicker elastic foundation thickness enhances stiffness and inertia, counteracting destabilizing aerodynamic effects, whereas thinner sections are more susceptible to instability. The results underline thickness optimization as a crucial design parameter for achieving robust aeroelastic performance in multiphase flow-driven pipe systems.

Fig. 15 examines the nonlinear aerodynamic flutter response of a gyroid-type TPMS composite pipe at $V_f = 2\ m/s$ and $\epsilon_G = 0.1$, focusing on the influence of Poisson's ratio of elastic foundation. The left subfigure shows the evolution of the imaginary part of frequency with respect to the aerodynamic pressure parameter. For low λ_∞, Ω_l remains close to unity across all cases, signifying stable oscillations. As λ_∞ increases, the frequencies split into two diverging branches, marking the classical flutter mechanism. Pipes with lower Poisson's ratio exhibit earlier bifurcation and lower critical λ_∞, indicating a reduced flutter threshold. Conversely, a higher Poisson's ratio delays the onset of instability, thereby enhancing aeroelastic stability. The right subfigure illustrates the variation of the real part of the frequency. At small λ_∞, Ω_R remains zero for all decreasing Poisson's ratio reduces effective stiffness in the circumferential direction, enhancing susceptibility to aerodynamic destabilization values, confirming stability. However, as λ_∞ rises, the branches diverge into positive and negative values, signifying instability onset. The divergence is sharper for a lower Poisson's ratio, meaning that pipes with greater lateral deformation tendencies are more prone to flutter instability. Physically, decreasing the Poisson's ratio reduces effective stiffness in the circumferential direction, enhancing susceptibility to aerodynamic destabilization. This figure highlights the sensitivity of aeroelastic stability to Poisson's ratio, emphasizing its importance in selecting TPMS material properties. Higher Poisson's ratio values provide superior resistance against flutter, a key insight for designing reliable composite pipes for multiphase flow applications under high aerodynamic loads.

Fig. 16 presents the effect of foundation stiffness on the nonlinear aerodynamic behavior of a gyroid-type TPMS composite pipe under constant aerodynamic pressure ($\lambda\infty = 100$), mixture velocity, and void fraction (ϵ_G= 0.1), while considering variations in both wall thickness ratio and Poisson's ratio. The left subfigure shows the influence of elastic foundation thickness on Ω_l as K_w increases. For all thicknesses, Ω_l rises monotonically with K_w, demonstrating that stronger foundations enhance system stability. Thicker elastic foundation exhibit higher Ω_l values across all K_w, whereas thinner walls yield lower values, confirming that structural stiffness significantly improves aeroelastic resistance. The right subfigure illustrates the effect of Poisson's ratio on Ω_R. Similar to thickness effects, Ω_R increases steadily with K_w. However, pipes with higher Poisson's ratio consistently display higher Ω_R values, confirming that reduced transverse deformation improves aeroelastic stability. At higher ν_f, the structure exhibits lower Ω_l, revealing greater vulnerability to destabilization even under stiffer foundations. Together, these results demonstrate a coupled dependency between foundation's thickness, Poisson's ratio, and foundation stiffness. Increasing

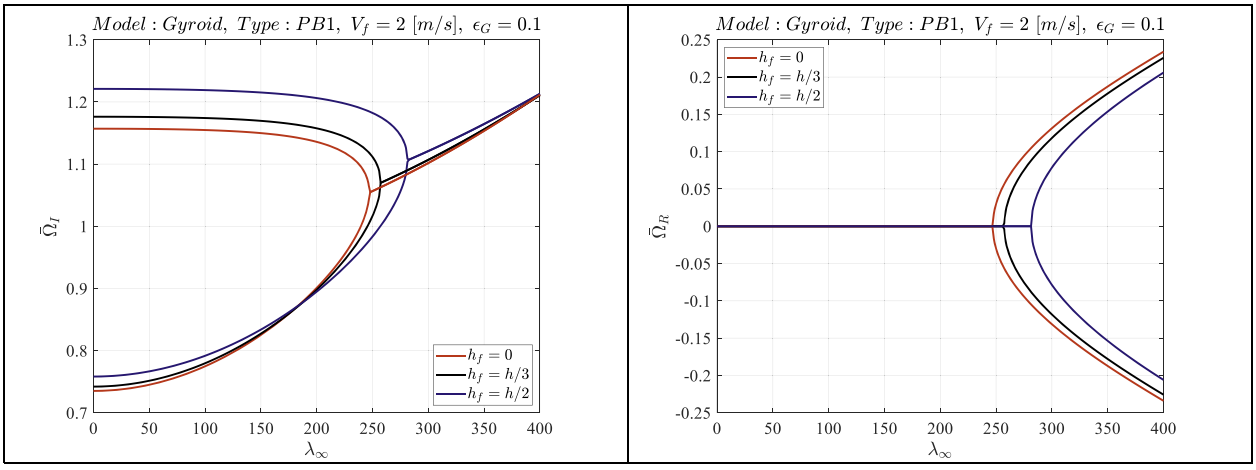

Fig. 14. The influence of pipe elastic foundation thickness ratio on the nonlinear aerodynamic flutter response of a gyroid-type TPMS composite pipe.

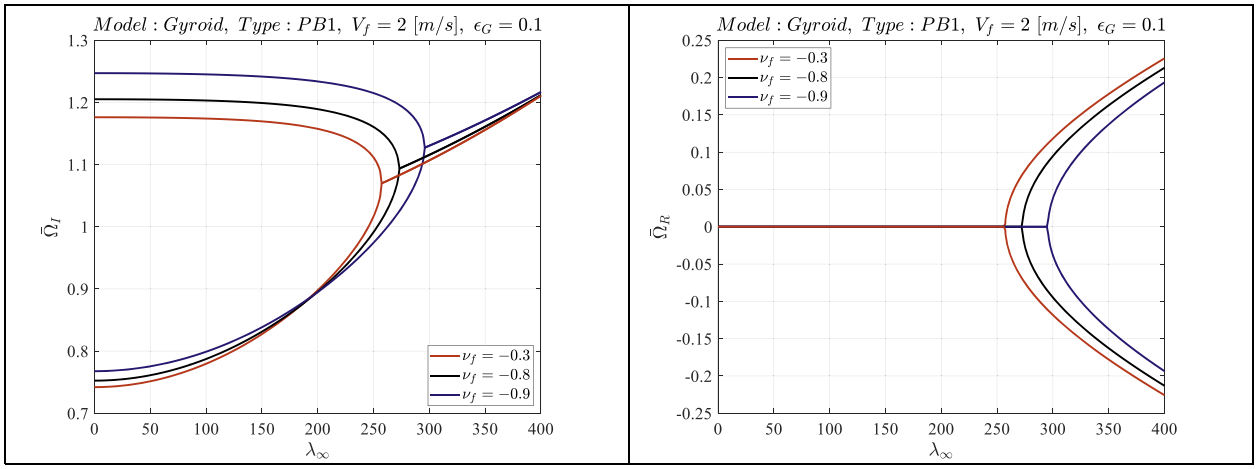

Fig. 15. The nonlinear aerodynamic flutter response of a gyroid-type TPMS composite pipe focusing on the influence of Poisson's ratio of elastic foundation.

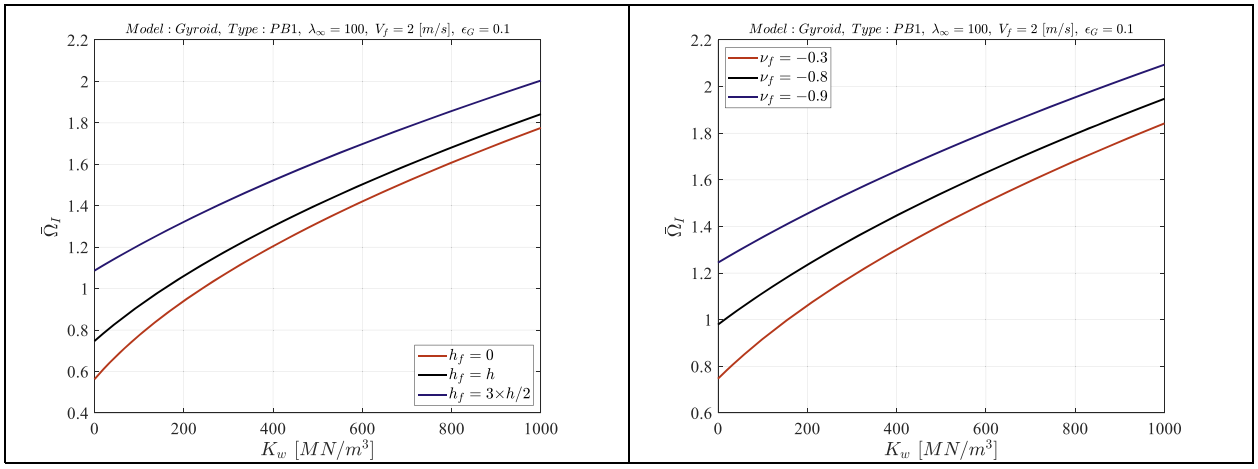

Fig. 16. The effect of auxetic foundation parameters on the nonlinear aerodynamic behavior of a gyroid-type TPMS composite pipe under constant aerodynamic pressure.

K_w systematically enhances flutter resistance, but this benefit is maximized when combined with thicker walls and higher ν_f values. Physically, the auxetic Winkler foundation provides restoring forces that delay instability, but intrinsic structural properties such as thickness and lateral deformability remain decisive factors. This figure underscores the multi-parameter optimization necessary to achieve robust aeroelastic stability in TPMS-reinforced pipes conveying two-phase flow.

Fig. 17 explores the influence of Winkler foundation stiffness on the natural frequency of a gyroid PB1 pipe subjected to aerodynamic loading, with $\lambda_\infty = 100$. Two-parameter studies are conducted: varying

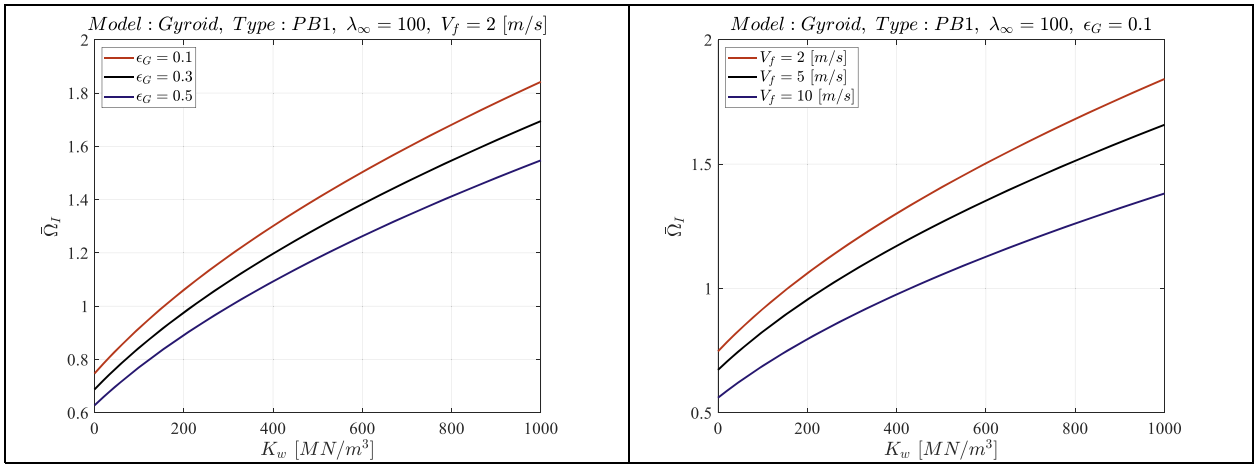

Fig. 17. The effect of various parameters on the nonlinear aerodynamic behavior of a gyroid-type TPMS composite pipe for different elastic foundation parameters.

gas void fraction and varying mixture velocity. The left panel examines Ω_I as a function of K_w for three void fractions, ϵ_G=0.1,0.3,0.5, at a constant flow velocity of $V_f = 2\ m/s$. Results show that natural frequency increases monotonically with foundation stiffness, confirming the stabilizing role of the auxetic support. However, higher void fractions reduce Ω_I, indicating that increased gas content lowers the effective density and stiffness of the two-phase medium, weakening the beneficial impact of K_w. The smallest void fraction provides the highest stability margin. The figure presents the effect of flow velocity ($V_f = 2,\ 5,\ 10\ m/s$) at a fixed void fraction of ϵ_G=0.1. Similar to the previous case, Ω_I rises with increasing K_w, emphasizing foundation reinforcement as a stabilizing mechanism. Yet, higher mixture velocities suppress Ω_I, reflecting stronger destabilizing aerodynamic contributions. For $V_f = 2\ m/s$, the system retains the highest natural frequencies across all K_w, while at $V_f = 10\ m/s$, the stabilizing influence of K_w is markedly reduced. Overall, Fig. 17 demonstrates that Winkler foundation stiffness significantly enhances natural frequency and postpones flutter, but its effect is limited when high void fractions or high velocities dominate system behavior.

Fig. 18 illustrates the dependence of the imaginary part of the natural frequency on the normalized foundation thickness ratio and the Poisson ratio for a gyroid-type TPMS pipe modeled under the PB1 configuration. The aerodynamic pressure parameter is set as $\lambda_\infty = 100$, and the mixture velocity is held constant at $V_f = 2\ m/s$. Three different gas void fractions are compared. The surface plots reveal that Ω_I is most sensitive to variations in void fraction, with higher void fractions significantly lowering the frequency response. This reduction indicates a destabilizing effect of increased gas content, which diminishes the effective stiffness and mass-carrying capacity of the composite structure. This interaction highlights that void fraction plays a dominant role in defining dynamic stability in two-phase reinforced systems.

Fig. 19 shows the response of Ω_I for the same gyroid PB1 model with $\lambda_\infty = 100$, but now the gas void fraction is fixed at $\epsilon_G = 0.1$. The comparison is made across three different mixture velocities: $V_f = 2, 5, 10\ m/s$. The surface maps demonstrate that as mixture velocity increases, the imaginary part of the frequency systematically decreases, indicating a higher susceptibility to aerodynamic flutter. The destabilizing role of flow velocity becomes more pronounced at negative υ_f, while positive ratios counteract this effect by enhancing system damping and delaying flutter onset. The results establish mixture velocity as a critical destabilizing parameter, consistent with aerodynamic theories of flutter. At low velocities, stability margins remain acceptable, but as velocity increases, the threshold for flutter pressure is approached more rapidly, narrowing the safe operating window.

5.3. The results of the presented hybrid machine learning algorithm

Hybrid DNNs are indeed a data-driven solution. In the context of structural dynamics, hybrid DNNs leverage large datasets containing information on various aspects of the system, such as geometry, material properties, loading conditions, and corresponding responses or behaviors. These datasets are used to train the DNN model, enabling it to learn complex relationships between input parameters and system responses. The term "data-driven" refers to the fact that hybrid DNNs derive their predictive capabilities primarily from the data they are trained on, rather than relying solely on analytical models or theoretical equations. The model learns patterns and relationships present in the data through iterative training processes, adjusting its internal parameters to minimize the difference between predicted and actual responses. By effectively capturing the underlying patterns in the data, hybrid DNNs can provide accurate predictions for various engineering problems, including estimating the frequency of structures such as pipes. An epoch in the context of machine learning, particularly for training a hybrid deep neural network, refers to a single complete pass through the entire training dataset by the learning algorithm. During an epoch, the model processes all training data in smaller batches (known as mini-batches) and updates its parameters, such as weights and biases, to minimize the error or loss function. Multiple epochs are typically required for the model to learn effectively, as a single pass may not fully capture the patterns in the data. The number of epochs is a hyperparameter that must be carefully chosen to balance underfitting and overfitting. In this study, the concept of epochs is crucial for ensuring that the hybrid DNN achieves sufficient accuracy and generalization for predicting the dynamic behavior of the composite pipe. This data-driven approach offers several advantages, including the ability to handle nonlinearities, adapt to diverse datasets, and provide rapid predictions once trained. The loss factor against various epochs for test, train, and validation sets is given in Fig. 20.

Comparing estimated results against measured data using various R^2

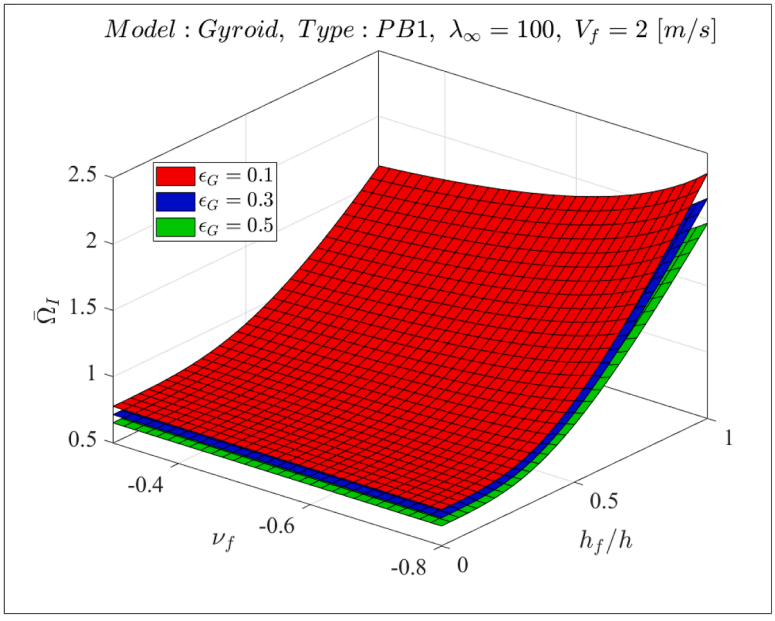

Fig. 18. The dependence of the imaginary part of the natural frequency on the normalized foundation thickness ratio and the Poisson ratio for a gyroid-type TPMS pipe modeled under the PB1 configuration different gas void fractions.

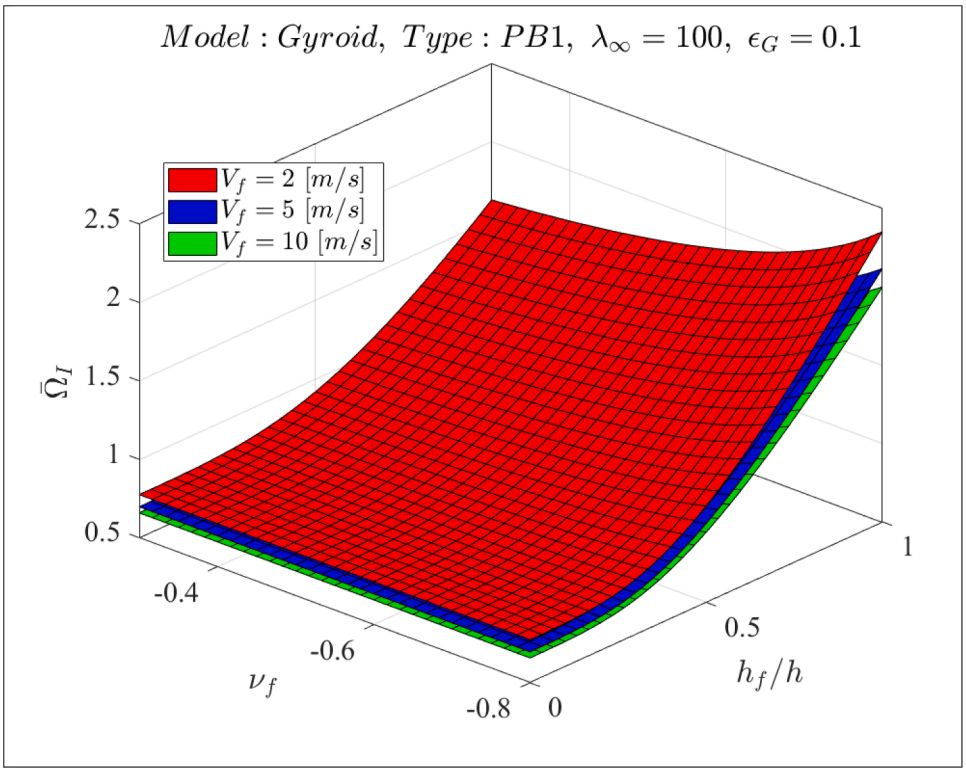

Fig. 19. The dependence of the imaginary part of the natural frequency on the normalized foundation thickness ratio and the Poisson ratio for a gyroid-type TPMS pipe modeled under the PB1 configuration and different mixture flow velocities.

parameters for hybrid deep neural networks serves as a critical evaluation of the model's predictive performance. The R^2 parameter, or coefficient of determination, measures the amount of variation in the dependent variable that can be predicted from the independent variables in a regression model. In the context of a hybrid DNN, which combines the strengths of different neural network architectures or integrates them with other machine learning techniques, assessing model accuracy through R^2 parameters provides insights into the model's ability to capture the underlying relationships in the data. The estimated against measured data for various R^2 parameters is given in Fig. 21. As shown by selecting R^2 equal to 0.9925, the results are fitted with each other.

This part now looks at how RMSE affected the outcomes, as seen in Table 6. The data suggests that answers with larger root mean square error (RMSE) parameters are more accurate. The 0.28691 value of the root mean square error can be used to establish the conclusions. Furthermore, the 4250 samples offer important support in this area.

Thus, the findings of the parametric research, Tables 6, previous figures, as well as the results of the provided hybrid DNN, are used to train the results. Consequently, it is determined that the input, hidden, and output layer configurations, together with an $RMSE_{Train}$ value of 0.28691 and an R^2 value of 0.9925, are appropriate for training the hybrid DNN prediction in this study. Table 7 displays the results of the most recent mathematical simulation using hybrid DNN to determine the dimensionless frequency of the structure that is being presented. It is seen that when the h_f/h parameter grows, and the present system's frequency decreases in the solution procedures as mentioned. Moreover, a shift in the volume ratio parameter from PB1 to PA1 is correlated with a decrease in the structure's frequency. Based on the data comparison, a significant degree of agreement between the two methods may be deduced.

6. Conclusion

In this work, for the first time, nonlinear aerodynamic responses of pipe conveying two-phase flow using data-driven solutions in the mathematical framework were presented. The presented pipe system was made of triply periodic minimum material with exceptional mechanical properties, such as high specific strength, specific stiffness, and energy absorption qualities. The distribution parameter varies as a function of the two-phase Reynolds number in a pipe while keeping the void percent constant and modifying the density ratios. Nonlinear Von-Karman theory, as well as general order shear deformation theory, was presented to correctly simulate the nonlinear aerodynamic responses of the pipe reinforced by triply periodic minimum material conveying two-phase flow. After that, a numerical solution procedure was used to solve the nonlinear governing equations with the aid of nonlinear boundary equations. After obtaining the dataset using the mathematical modeling section, the data-driven solution was used to correctly test, train, and validate the results for simulating the current applicable structure in other complex situations. The following gold points can be achieved from the results section:

- Ø As the aerodynamic pressure increases, the imaginary part of the frequency corresponding to the first mode increases significantly for the "Gyroid" model, while it remains more stable for the "Primitive" and "IWP" models.
- Ø The PB1 type shows the most significant shift in the real and imaginary parts of the frequencies as λ_∞ increases, indicating a higher sensitivity to aerodynamic pressure.
- Ø Comparing the TPMS types, PB3 exhibits the most favorable damping behavior, while PB1 shows earlier degradation of stability.
- Ø Higher mixture velocities shift the critical flutter boundary to lower λ_∞ values, meaning that pipes conveying faster two-phase flows are more prone to flutter instability.

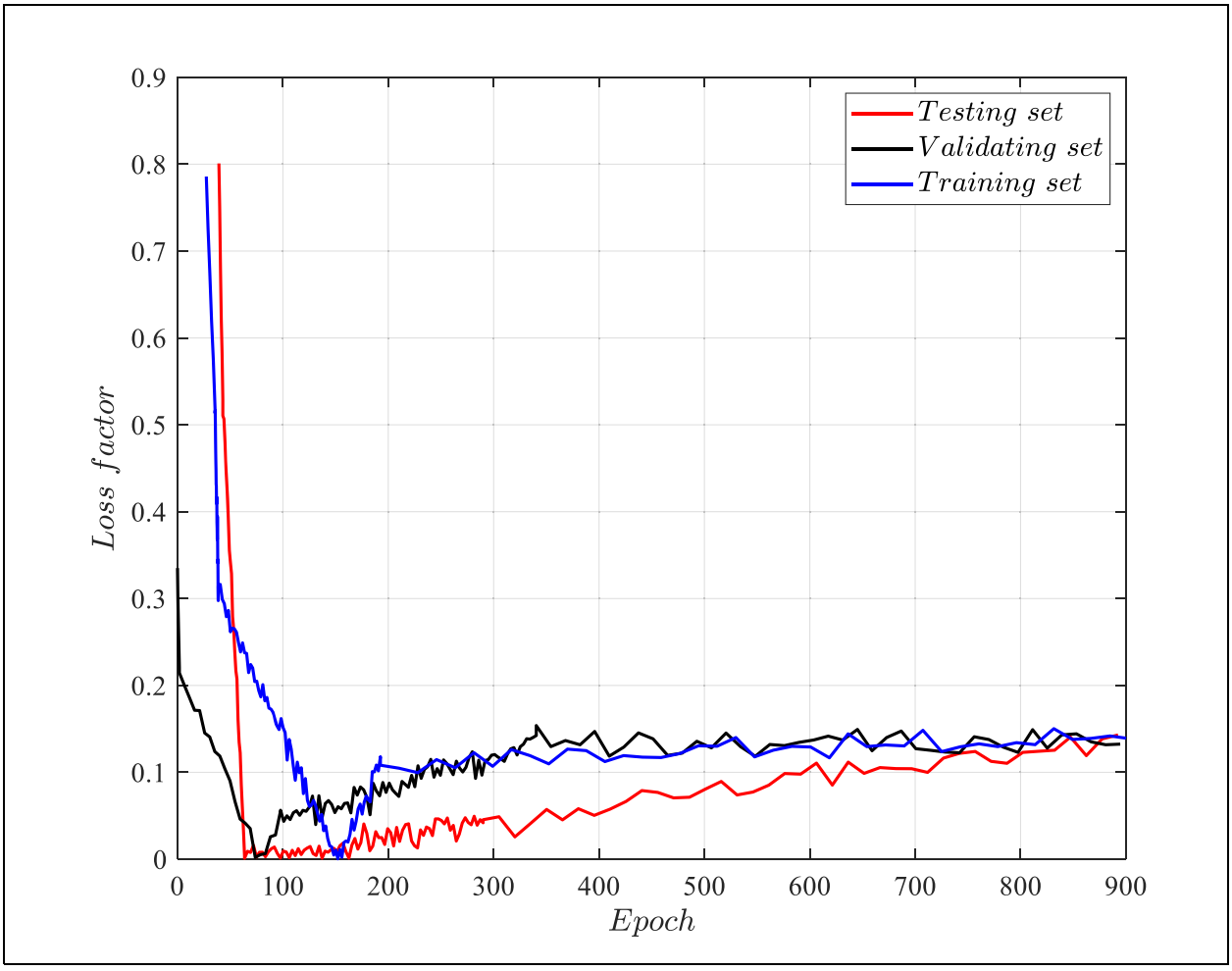

Fig. 20. Loss factor against various epochs for test, train, and validation sets.

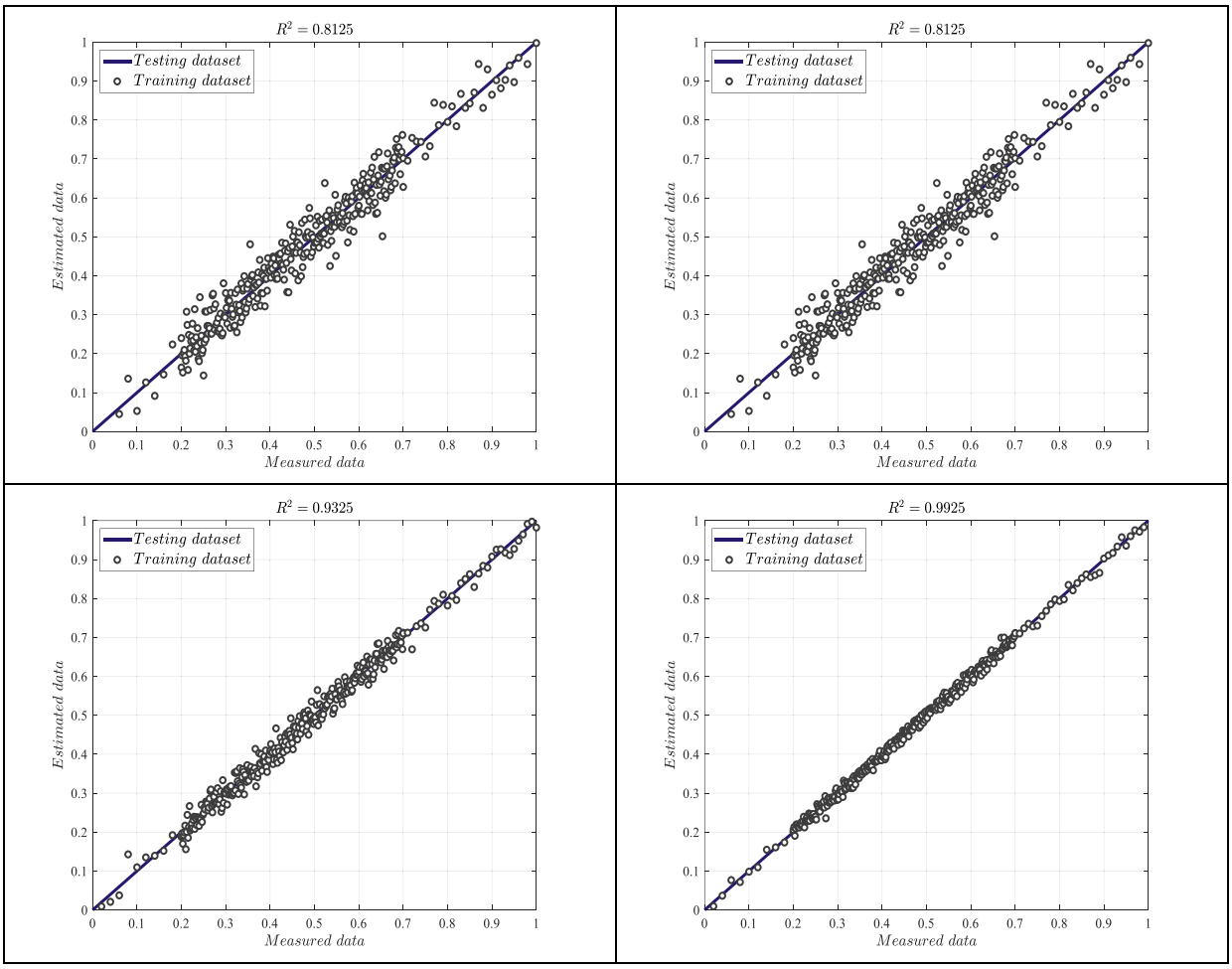

Fig. 21. Estimated against measured data for various R^2 parameters.

Table 6
Hybrid DNN model performance for dimensionless frequency for different RMSE and h_f/h values.

h_f/h	Fitted value	Predicted		
		$RMSE_{Train}$ = 0.17523	$RMSE_{Train}$ = 0.25693	$RMSE_{Train}$ = 0.28691
1/3	1.74761	2.57342	1.9376	1.74765
1/4	1.53263	2.15665	1.71461	1.53227
1/5	1.14375	1.77241	1.39755	1.14301
1/6	0.563527	1.04339	0.644934	0.563576
0	0.233415	0.413334	0.275337	0.233604

Table 7
Comparing the dimensionless frequency of a pipe via hybrid DNN and mathematics simulation results by varying the h_f/h and volume ratio parameters.

h_f/h	Volume ratio			
	*PA*1		*PB*1	
	Mathematics	Hybrid DNN	Mathematics	Hybrid DNN
1/3	0.994995	0.994905	1.74761	1.74631
1/4	0.872211	0.872111	1.53263	1.53257
1/5	0.651709	0.651618	1.14375	1.14383
1/6	0.323042	0.323001	0.563527	0.563518

- Ø The void fraction plays a decisive role in governing flutter behavior, with higher gas content significantly lowering the stability threshold.
- Ø The input, hidden, and output layer configurations, together with an $RMSE_{Train}$ value of 0.28691 and an R^2 value of 0.9925, are appropriate for training the hybrid DNN prediction in this study.
- Ø A stiffer foundation provides greater resistance to aeroelastic excitation, effectively postponing the onset of flutter and reducing the amplitude of unstable oscillations.
- Ø Thicker elastic foundation thickness enhances stiffness and inertia, counteracting destabilizing aerodynamic effects, whereas thinner sections are more susceptible to instability.
- Ø Pipes with a lower Poisson's ratio exhibit earlier bifurcation and lower critical λ_∞, indicating a reduced flutter threshold.
- Ø Increasing K_w systematically enhances flutter resistance, but this benefit is maximized when combined with thicker walls and higher ν_f values.

CRediT authorship contribution statement

Yujun Cao: Writing – review & editing, Writing – original draft, Visualization, Validation, Supervision, Software, Resources, Project administration, Methodology, Investigation. **Mohammed El-Meligy:** Writing – review & editing, Writing – original draft, Visualization, Validation, Software, Resources, Methodology, Investigation. **Mubariz Garayev:** Writing – original draft, Visualization, Validation, Software, Resources, Methodology, Investigation.

Declaration of competing interest

The authors declare that they have no conflict of interest.

Acknowledgement

The authors extend their appreciation to King Saud University for funding this work through the Ongoing Research Funding program, **(ORF-2025-1056)**, King Saud University, Riyadh, Saudi Arabia.

Appendix

The following relations are obtained by substituting Eqs. (19a-d), (20), and (21) into Eq. (16).

$$\delta u_0 : \frac{\partial N_{xx}^{(0)}}{\partial x}+\frac{1}{R}\frac{\partial N_{x\theta}^{(0)}}{\partial \theta}=\left(\left(I_{0p}^{(0)}+I_{0L}^{(0)}+I_{0G}^{(0)}\right)\frac{\partial^2 u_0}{\partial t^2}+\left(I_{1p}^{(0)}+I_{1L}^{(0)}+I_{1G}^{(0)}\right)\frac{\partial^2 u_1}{\partial t^2}+\left(I_{2p}^{(0)}+I_{2L}^{(0)}+I_{2G}^{(0)}\right)\frac{\partial^2 u_2}{\partial t^2}+\left(I_{3p}^{(0)}+I_{3L}^{(0)}+I_{3G}^{(0)}\right)\frac{\partial^2 u_3}{\partial t^2}\right)$$
$$+\left(\left(2V_LI_{0L}^{(0)}+2V_GI_{0G}^{(0)}\right)\frac{\partial^2 u_0}{\partial x\partial t}+\left(2V_LI_{1L}^{(0)}+2V_GI_{1G}^{(0)}\right)\frac{\partial^2 u_1}{\partial x\partial t}+\left(2V_LI_{2L}^{(0)}+2V_GI_{2G}^{(0)}\right)\frac{\partial^2 u_2}{\partial x\partial t}+\left(2V_LI_{3L}^{(0)}+2V_GI_{3G}^{(0)}\right)\frac{\partial^2 u_3}{\partial x\partial t}\right) \quad (A1)$$
$$+\left(\left(V_L^2I_{0L}^{(0)}+V_G^2I_{0G}^{(0)}\right)\frac{\partial^2 u_0}{\partial x^2}+\left(V_L^2I_{1L}^{(0)}+V_G^2I_{1G}^{(0)}\right)\frac{\partial^2 u_1}{\partial x^2}+\left(V_L^2I_{2L}^{(0)}+V_G^2I_{2G}^{(0)}\right)\frac{\partial^2 u_2}{\partial x^2}+\left(V_L^2I_{3L}^{(0)}+V_G^2I_{3G}^{(0)}\right)\frac{\partial^2 u_3}{\partial x^2}\right)$$

$$\delta v_0 : \frac{1}{R}\frac{\partial N_{\theta\theta}^{(0)}}{\partial \theta}+\frac{\partial N_{x\theta}^{(0)}}{\partial x}==\left(\left(I_{0p}^{(0)}+I_{0L}^{(0)}+I_{0G}^{(0)}\right)\frac{\partial^2 v_0}{\partial t^2}+\left(I_{1p}^{(0)}+I_{1L}^{(0)}+I_{1G}^{(0)}\right)\frac{\partial^2 v_1}{\partial t^2}+\left(I_{2p}^{(0)}+I_{2L}^{(0)}+I_{2G}^{(0)}\right)\frac{\partial^2 v_2}{\partial t^2}+\left(I_{3p}^{(0)}+I_{3L}^{(0)}+I_{3G}^{(0)}\right)\frac{\partial^2 v_3}{\partial t^2}\right)$$
$$+\left(\left(2V_LI_{0L}^{(0)}+2V_GI_{0G}^{(0)}\right)\frac{\partial^2 v_0}{\partial x\partial t}+\left(2V_LI_{1L}^{(0)}+2V_GI_{1G}^{(0)}\right)\frac{\partial^2 v_1}{\partial x\partial t}+\left(2V_LI_{2L}^{(0)}+2V_GI_{2G}^{(0)}\right)\frac{\partial^2 v_2}{\partial x\partial t}+\left(2V_LI_{3L}^{(0)}+2V_GI_{3G}^{(0)}\right)\frac{\partial^2 v_3}{\partial x\partial t}\right) \quad (A2)$$
$$+\left(\left(V_L^2I_{0L}^{(0)}+V_G^2I_{0G}^{(0)}\right)\frac{\partial^2 v_0}{\partial x^2}+\left(V_L^2I_{1L}^{(0)}+V_G^2I_{1G}^{(0)}\right)\frac{\partial^2 v_1}{\partial x^2}+\left(V_L^2I_{2L}^{(0)}+V_G^2I_{2G}^{(0)}\right)\frac{\partial^2 v_2}{\partial x^2}+\left(V_L^2I_{3L}^{(0)}+V_G^2I_{3G}^{(0)}\right)\frac{\partial^2 v_3}{\partial x^2}\right)$$

$$\delta w_0 : \frac{1}{R}\frac{\partial N_{\theta z}^{(0)}}{\partial \theta}+\frac{\partial N_{xz}^{(0)}}{\partial x}+\frac{\partial}{\partial x}\left(N_{xx}^{(0)}\frac{\partial w_0}{\partial x}\right)+\frac{1}{R^2}\frac{\partial}{\partial \theta}\left(N_{\theta\theta}^{(0)}\frac{\partial w_0}{\partial \theta}\right)+\frac{1}{2R}\frac{\partial}{\partial x}\left(N_{x\theta}^{(0)}\frac{\partial w_0}{\partial \theta}\right)+\frac{1}{2R}\frac{\partial}{\partial \theta}\left(N_{x\theta}^{(0)}\frac{\partial w_0}{\partial x}\right)$$
$$-\Delta P-K_w\left(w_0+\left(\frac{h}{2}\right)w_1+\frac{h^2}{2^2\times 2!}w_2+\frac{h^3}{2^3\times 3!}w_3\right)+D_f\nabla^4\left(w_0+\left(\frac{h}{2}\right)w_1+\frac{h^2}{2^2\times 2!}w_2+\frac{h^3}{2^3\times 3!}w_3\right)$$
$$=\left(\left(I_{0p}^{(0)}+I_{0L}^{(0)}+I_{0G}^{(0)}\right)\frac{\partial^2 w_0}{\partial t^2}+\left(I_{1p}^{(0)}+I_{1L}^{(0)}+I_{1G}^{(0)}\right)\frac{\partial^2 w_1}{\partial t^2}+\left(I_{2p}^{(0)}+I_{2L}^{(0)}+I_{2G}^{(0)}\right)\frac{\partial^2 w_2}{\partial t^2}+\left(I_{3p}^{(0)}+I_{3L}^{(0)}+I_{3G}^{(0)}\right)\frac{\partial^2 w_3}{\partial t^2}\right) \quad (A3)$$
$$+\left(\left(2V_LI_{0L}^{(0)}+2V_GI_{0G}^{(0)}\right)\frac{\partial^2 w_0}{\partial x\partial t}+\left(2V_LI_{1L}^{(0)}+2V_GI_{1G}^{(0)}\right)\frac{\partial^2 w_1}{\partial x\partial t}+\left(2V_LI_{2L}^{(0)}+2V_GI_{2G}^{(0)}\right)\frac{\partial^2 w_2}{\partial x\partial t}+\left(2V_LI_{3L}^{(0)}+2V_GI_{3G}^{(0)}\right)\frac{\partial^2 w_3}{\partial x\partial t}\right)$$
$$+\left(\left(V_L^2I_{0L}^{(0)}+V_G^2I_{0G}^{(0)}\right)\frac{\partial^2 w_0}{\partial x^2}+\left(V_L^2I_{1L}^{(0)}+V_G^2I_{1G}^{(0)}\right)\frac{\partial^2 w_1}{\partial x^2}+\left(V_L^2I_{2L}^{(0)}+V_G^2I_{2G}^{(0)}\right)\frac{\partial^2 w_2}{\partial x^2}+\left(V_L^2I_{3L}^{(0)}+V_G^2I_{3G}^{(0)}\right)\frac{\partial^2 w_3}{\partial x^2}\right)$$

$$\delta u_1 : \frac{\partial N_{xx}^{(1)}}{\partial x}+\frac{1}{R}\frac{\partial N_{x\theta}^{(1)}}{\partial \theta}-N_{xz}^{(0)}=\left(\left(I_{0p}^{(1)}+I_{0L}^{(1)}+I_{0G}^{(1)}\right)\frac{\partial^2 u_0}{\partial t^2}+\left(I_{1p}^{(1)}+I_{1L}^{(1)}+I_{1G}^{(1)}\right)\frac{\partial^2 u_1}{\partial t^2}+\left(I_{2p}^{(1)}+I_{2L}^{(1)}+I_{2G}^{(1)}\right)\frac{\partial^2 u_2}{\partial t^2}+\left(I_{3p}^{(1)}+I_{3L}^{(1)}+I_{3G}^{(1)}\right)\frac{\partial^2 u_3}{\partial t^2}\right)$$
$$+\left(\left(2V_LI_{0L}^{(1)}+2V_GI_{0G}^{(1)}\right)\frac{\partial^2 u_0}{\partial x\partial t}+\left(2V_LI_{1L}^{(1)}+2V_GI_{1G}^{(1)}\right)\frac{\partial^2 u_1}{\partial x\partial t}+\left(2V_LI_{2L}^{(1)}+2V_GI_{2G}^{(1)}\right)\frac{\partial^2 u_2}{\partial x\partial t}+\left(2V_LI_{3L}^{(1)}+2V_GI_{3G}^{(1)}\right)\frac{\partial^2 u_3}{\partial x\partial t}\right) \quad (A4)$$
$$+\left(\left(V_L^2I_{0L}^{(1)}+V_G^2I_{0G}^{(1)}\right)\frac{\partial^2 u_0}{\partial x^2}+\left(V_L^2I_{1L}^{(1)}+V_G^2I_{1G}^{(1)}\right)\frac{\partial^2 u_1}{\partial x^2}+\left(V_L^2I_{2L}^{(1)}+V_G^2I_{2G}^{(1)}\right)\frac{\partial^2 u_2}{\partial x^2}+\left(V_L^2I_{3L}^{(1)}+V_G^2I_{3G}^{(1)}\right)\frac{\partial^2 u_3}{\partial x^2}\right)$$

$$\delta v_1 : \frac{1}{R}\frac{\partial N_{\theta\theta}^{(1)}}{\partial \theta} + \frac{\partial N_{x\theta}^{(1)}}{\partial x} - N_{\theta z}^{(0)} = \left(\left(I_{0p}^{(1)} + I_{0L}^{(1)} + I_{0G}^{(1)}\right)\frac{\partial^2 v_0}{\partial t^2} + \left(I_{1p}^{(1)} + I_{1L}^{(1)} + I_{1G}^{(1)}\right)\frac{\partial^2 v_1}{\partial t^2} + \left(I_{2p}^{(1)} + I_{2L}^{(1)} + I_{2G}^{(1)}\right)\frac{\partial^2 v_2}{\partial t^2} + \left(I_{3p}^{(1)} + I_{3L}^{(1)} + I_{3G}^{(1)}\right)\frac{\partial^2 v_3}{\partial t^2}\right)$$
$$+\left(\left(2V_L I_{0L}^{(1)} + 2V_G I_{0G}^{(1)}\right)\frac{\partial^2 v_0}{\partial x \partial t} + \left(2V_L I_{1L}^{(1)} + 2V_G I_{1G}^{(1)}\right)\frac{\partial^2 v_1}{\partial x \partial t} + \left(2V_L I_{2L}^{(1)} + 2V_G I_{2G}^{(1)}\right)\frac{\partial^2 v_2}{\partial x \partial t} + \left(2V_L I_{3L}^{(1)} + 2V_G I_{3G}^{(1)}\right)\frac{\partial^2 v_3}{\partial x \partial t}\right) \tag{A5}$$
$$+\left(\left(V_L^2 I_{0L}^{(1)} + V_G^2 I_{0G}^{(1)}\right)\frac{\partial^2 v_0}{\partial x^2} + \left(V_L^2 I_{1L}^{(1)} + V_G^2 I_{1G}^{(1)}\right)\frac{\partial^2 v_1}{\partial x^2} + \left(V_L^2 I_{2L}^{(1)} + V_G^2 I_{2G}^{(1)}\right)\frac{\partial^2 v_2}{\partial x^2} + \left(V_L^2 I_{3L}^{(1)} + V_G^2 I_{3G}^{(1)}\right)\frac{\partial^2 v_3}{\partial x^2}\right)$$

$$\delta W_1 : \frac{1}{R}\frac{\partial N_{\theta z}^{(1)}}{\partial \theta} + \frac{\partial N_{xz}^{(1)}}{\partial x} - N_{zz}^{(0)} + \left(\frac{h}{2}\right) \times \left(-\Delta P - K_w\left(w_0 + \left(\frac{h}{2}\right)w_1 + \frac{h^2}{2^2 \times 2!}w_2 + \frac{h^3}{2^3 \times 3!}w_3\right) + D_f \nabla^4 \left(w_0 + \left(\frac{h}{2}\right)w_1 + \frac{h^2}{2^2 \times 2!}w_2 + \frac{h^3}{2^3 \times 3!}w_3\right)\right)$$
$$= \left(\left(I_{0p}^{(1)} + I_{0L}^{(1)} + I_{0G}^{(1)}\right)\frac{\partial^2 w_0}{\partial t^2} + \left(I_{1p}^{(1)} + I_{1L}^{(1)} + I_{1G}^{(1)}\right)\frac{\partial^2 w_1}{\partial t^2} + \left(I_{2p}^{(1)} + I_{2L}^{(1)} + I_{2G}^{(1)}\right)\frac{\partial^2 w_2}{\partial t^2} + \left(I_{3p}^{(1)} + I_{3L}^{(1)} + I_{3G}^{(1)}\right)\frac{\partial^2 w_3}{\partial t^2}\right)$$
$$+\left(\left(2V_L I_{0L}^{(1)} + 2V_G I_{0G}^{(1)}\right)\frac{\partial^2 w_0}{\partial x \partial t} + \left(2V_L I_{1L}^{(1)} + 2V_G I_{1G}^{(1)}\right)\frac{\partial^2 w_1}{\partial x \partial t} + \left(2V_L I_{2L}^{(1)} + 2V_G I_{2G}^{(1)}\right)\frac{\partial^2 w_2}{\partial x \partial t} + \left(2V_L I_{3L}^{(1)} + 2V_G I_{3G}^{(1)}\right)\frac{\partial^2 w_3}{\partial x \partial t}\right)$$
$$+\left(\left(V_L^2 I_{0L}^{(1)} + V_G^2 I_{0G}^{(1)}\right)\frac{\partial^2 w_0}{\partial x^2} + \left(V_L^2 I_{1L}^{(1)} + V_G^2 I_{1G}^{(1)}\right)\frac{\partial^2 w_1}{\partial x^2} + \left(V_L^2 I_{2L}^{(1)} + V_G^2 I_{2G}^{(1)}\right)\frac{\partial^2 w_2}{\partial x^2} + \left(V_L^2 I_{3L}^{(1)} + V_G^2 I_{3G}^{(1)}\right)\frac{\partial^2 w_3}{\partial x^2}\right) \tag{A6}$$

$$\delta u_2 : \frac{\partial N_{xx}^{(2)}}{\partial x} + \frac{1}{R}\frac{\partial N_{x\theta}^{(2)}}{\partial \theta} - N_{xz}^{(1)} = \left(\left(I_{0p}^{(2)} + I_{0L}^{(2)} + I_{0G}^{(2)}\right)\frac{\partial^2 u_0}{\partial t^2} + \left(I_{1p}^{(2)} + I_{1L}^{(2)} + I_{1G}^{(2)}\right)\frac{\partial^2 u_1}{\partial t^2} + \left(I_{2p}^{(2)} + I_{2L}^{(2)} + I_{2G}^{(2)}\right)\frac{\partial^2 u_2}{\partial t^2} + \left(I_{3p}^{(2)} + I_{3L}^{(2)} + I_{3G}^{(2)}\right)\frac{\partial^2 u_3}{\partial t^2}\right)$$
$$+\left(\left(2V_L I_{0L}^{(2)} + 2V_G I_{0G}^{(2)}\right)\frac{\partial^2 u_0}{\partial x \partial t} + \left(2V_L I_{1L}^{(2)} + 2V_G I_{1G}^{(2)}\right)\frac{\partial^2 u_1}{\partial x \partial t} + \left(2V_L I_{2L}^{(2)} + 2V_G I_{2G}^{(2)}\right)\frac{\partial^2 u_2}{\partial x \partial t} + \left(2V_L I_{3L}^{(2)} + 2V_G I_{3G}^{(2)}\right)\frac{\partial^2 u_3}{\partial x \partial t}\right) \tag{A7}$$
$$+\left(\left(V_L^2 I_{0L}^{(2)} + V_G^2 I_{0G}^{(2)}\right)\frac{\partial^2 u_0}{\partial x^2} + \left(V_L^2 I_{1L}^{(2)} + V_G^2 I_{1G}^{(2)}\right)\frac{\partial^2 u_1}{\partial x^2} + \left(V_L^2 I_{2L}^{(2)} + V_G^2 I_{2G}^{(2)}\right)\frac{\partial^2 u_2}{\partial x^2} + \left(V_L^2 I_{3L}^{(2)} + V_G^2 I_{3G}^{(2)}\right)\frac{\partial^2 u_3}{\partial x^2}\right)$$

$$\delta v_2 : \frac{1}{R}\frac{\partial N_{\theta\theta}^{(2)}}{\partial \theta} + \frac{\partial N_{x\theta}^{(2)}}{\partial x} - N_{\theta z}^{(1)} = \left(\left(I_{0p}^{(2)} + I_{0L}^{(2)} + I_{0G}^{(2)}\right)\frac{\partial^2 v_0}{\partial t^2} + \left(I_{1p}^{(2)} + I_{1L}^{(2)} + I_{1G}^{(2)}\right)\frac{\partial^2 v_1}{\partial t^2} + \left(I_{2p}^{(2)} + I_{2L}^{(2)} + I_{2G}^{(2)}\right)\frac{\partial^2 v_2}{\partial t^2} + \left(I_{3p}^{(2)} + I_{3L}^{(2)} + I_{3G}^{(2)}\right)\frac{\partial^2 v_3}{\partial t^2}\right)$$
$$+\left(\left(2V_L I_{0L}^{(2)} + 2V_G I_{0G}^{(2)}\right)\frac{\partial^2 v_0}{\partial x \partial t} + \left(2V_L I_{1L}^{(2)} + 2V_G I_{1G}^{(2)}\right)\frac{\partial^2 v_1}{\partial x \partial t} + \left(2V_L I_{2L}^{(2)} + 2V_G I_{2G}^{(2)}\right)\frac{\partial^2 v_2}{\partial x \partial t} + \left(2V_L I_{3L}^{(2)} + 2V_G I_{3G}^{(2)}\right)\frac{\partial^2 v_3}{\partial x \partial t}\right) \tag{A8}$$
$$+\left(\left(V_L^2 I_{0L}^{(2)} + V_G^2 I_{0G}^{(2)}\right)\frac{\partial^2 v_0}{\partial x^2} + \left(V_L^2 I_{1L}^{(2)} + V_G^2 I_{1G}^{(2)}\right)\frac{\partial^2 v_1}{\partial x^2} + \left(V_L^2 I_{2L}^{(2)} + V_G^2 I_{2G}^{(2)}\right)\frac{\partial^2 v_2}{\partial x^2} + \left(V_L^2 I_{3L}^{(2)} + V_G^2 I_{3G}^{(2)}\right)\frac{\partial^2 v_3}{\partial x^2}\right)$$

$$\delta W_2 : \frac{1}{R}\frac{\partial N_{\theta z}^{(2)}}{\partial \theta} + \frac{\partial N_{xz}^{(2)}}{\partial x} - N_{zz}^{(1)} + \left(\frac{h^2}{2^2 \times 2!}\right) \times \times \left(-\Delta P - K_w\left(w_0 + \left(\frac{h}{2}\right)w_1 + \frac{h^2}{2^2 \times 2!}w_2 + \frac{h^3}{2^3 \times 3!}w_3\right) + D_f \nabla^4 \left(w_0 + \left(\frac{h}{2}\right)w_1 + \frac{h^2}{2^2 \times 2!}w_2 + \frac{h^3}{2^3 \times 3!}w_3\right)\right)$$
$$= \left(\left(I_{0p}^{(2)} + I_{0L}^{(2)} + I_{0G}^{(2)}\right)\frac{\partial^2 w_0}{\partial t^2} + \left(I_{1p}^{(2)} + I_{1L}^{(2)} + I_{1G}^{(2)}\right)\frac{\partial^2 w_1}{\partial t^2} + \left(I_{2p}^{(2)} + I_{2L}^{(2)} + I_{2G}^{(2)}\right)\frac{\partial^2 w_2}{\partial t^2} + \left(I_{3p}^{(2)} + I_{3L}^{(2)} + I_{3G}^{(2)}\right)\frac{\partial^2 w_3}{\partial t^2}\right)$$
$$+\left(\left(2V_L I_{0L}^{(2)} + 2V_G I_{0G}^{(2)}\right)\frac{\partial^2 w_0}{\partial x \partial t} + \left(2V_L I_{1L}^{(2)} + 2V_G I_{1G}^{(2)}\right)\frac{\partial^2 w_1}{\partial x \partial t} + \left(2V_L I_{2L}^{(2)} + 2V_G I_{2G}^{(2)}\right)\frac{\partial^2 w_2}{\partial x \partial t} + \left(2V_L I_{3L}^{(2)} + 2V_G I_{3G}^{(2)}\right)\frac{\partial^2 w_3}{\partial x \partial t}\right)$$
$$+\left(\left(V_L^2 I_{0L}^{(2)} + V_G^2 I_{0G}^{(2)}\right)\frac{\partial^2 w_0}{\partial x^2} + \left(V_L^2 I_{1L}^{(2)} + V_G^2 I_{1G}^{(2)}\right)\frac{\partial^2 w_1}{\partial x^2} + \left(V_L^2 I_{2L}^{(2)} + V_G^2 I_{2G}^{(2)}\right)\frac{\partial^2 w_2}{\partial x^2} + \left(V_L^2 I_{3L}^{(2)} + V_G^2 I_{3G}^{(2)}\right)\frac{\partial^2 w_3}{\partial x^2}\right) \tag{A9}$$

$$\delta u_3 : \frac{\partial N_{xx}^{(3)}}{\partial x} + \frac{1}{R}\frac{\partial N_{x\theta}^{(3)}}{\partial \theta} - N_{xz}^{(2)} = \left(\left(I_{0p}^{(3)} + I_{0L}^{(3)} + I_{0G}^{(3)}\right)\frac{\partial^2 u_0}{\partial t^2} + \left(I_{1p}^{(3)} + I_{1L}^{(3)} + I_{1G}^{(3)}\right)\frac{\partial^2 u_1}{\partial t^2} + \left(I_{2p}^{(3)} + I_{2L}^{(3)} + I_{2G}^{(3)}\right)\frac{\partial^2 u_2}{\partial t^2} + \left(I_{3p}^{(3)} + I_{3L}^{(3)} + I_{3G}^{(3)}\right)\frac{\partial^2 u_3}{\partial t^2}\right)$$
$$+\left(\left(2V_L I_{0L}^{(3)} + 2V_G I_{0G}^{(3)}\right)\frac{\partial^2 u_0}{\partial x \partial t} + \left(2V_L I_{1L}^{(3)} + 2V_G I_{1G}^{(3)}\right)\frac{\partial^2 u_1}{\partial x \partial t} + \left(2V_L I_{2L}^{(3)} + 2V_G I_{2G}^{(3)}\right)\frac{\partial^2 u_2}{\partial x \partial t} + \left(2V_L I_{3L}^{(3)} + 2V_G I_{3G}^{(3)}\right)\frac{\partial^2 u_3}{\partial x \partial t}\right) \tag{A10}$$
$$+\left(\left(V_L^2 I_{0L}^{(3)} + V_G^2 I_{0G}^{(3)}\right)\frac{\partial^2 u_0}{\partial x^2} + \left(V_L^2 I_{1L}^{(3)} + V_G^2 I_{1G}^{(3)}\right)\frac{\partial^2 u_1}{\partial x^2} + \left(V_L^2 I_{2L}^{(3)} + V_G^2 I_{2G}^{(3)}\right)\frac{\partial^2 u_2}{\partial x^2} + \left(V_L^2 I_{3L}^{(3)} + V_G^2 I_{3G}^{(3)}\right)\frac{\partial^2 u_3}{\partial x^2}\right)$$

$$\delta v_3 : \frac{1}{R}\frac{\partial N_{\theta\theta}^{(3)}}{\partial \theta} + \frac{\partial N_{x\theta}^{(3)}}{\partial x} - N_{\theta z}^{(2)} = \left(\left(I_{0p}^{(3)} + I_{0L}^{(3)} + I_{0G}^{(3)}\right)\frac{\partial^2 v_0}{\partial t^2} + \left(I_{1p}^{(3)} + I_{1L}^{(3)} + I_{1G}^{(3)}\right)\frac{\partial^2 v_1}{\partial t^2} + \left(I_{2p}^{(3)} + I_{2L}^{(3)} + I_{2G}^{(3)}\right)\frac{\partial^2 v_2}{\partial t^2} + \left(I_{3p}^{(3)} + I_{3L}^{(3)} + I_{3G}^{(3)}\right)\frac{\partial^2 v_3}{\partial t^2}\right)$$
$$+\left(\left(2V_L I_{0L}^{(3)} + 2V_G I_{0G}^{(3)}\right)\frac{\partial^2 v_0}{\partial x \partial t} + \left(2V_L I_{1L}^{(3)} + 2V_G I_{1G}^{(3)}\right)\frac{\partial^2 v_1}{\partial x \partial t} + \left(2V_L I_{2L}^{(3)} + 2V_G I_{2G}^{(3)}\right)\frac{\partial^2 v_2}{\partial x \partial t} + \left(2V_L I_{3L}^{(3)} + 2V_G I_{3G}^{(3)}\right)\frac{\partial^2 v_3}{\partial x \partial t}\right) \tag{A11}$$
$$\left(\left(V_L^2 I_{0L}^{(3)} + V_G^2 I_{0G}^{(3)}\right)\frac{\partial^2 v_0}{\partial x^2} + \left(V_L^2 I_{1L}^{(3)} + V_G^2 I_{1G}^{(3)}\right)\frac{\partial^2 v_1}{\partial x^2} + \left(V_L^2 I_{2L}^{(3)} + V_G^2 I_{2G}^{(3)}\right)\frac{\partial^2 v_2}{\partial x^2} + \left(V_L^2 I_{3L}^{(3)} + V_G^2 I_{3G}^{(3)}\right)\frac{\partial^2 v_3}{\partial x^2}\right)$$

$$\delta W_3 : \frac{1}{R}\frac{\partial N_{\theta z}^{(3)}}{\partial \theta}+\frac{\partial N_{xz}^{(3)}}{\partial x}-N_{zz}^{(2)}+\left(\frac{h^3}{2^3\times 3!}\right)\times\times\left(-\Delta P-K_w\left(w_0+\left(\frac{h}{2}\right)w_1+\frac{h^2}{2^2\times 2!}w_2+\frac{h^3}{2^3\times 3!}w_3\right)+D_f\nabla^4\left(w_0+\left(\frac{h}{2}\right)w_1+\frac{h^2}{2^2\times 2!}w_2+\frac{h^3}{2^3\times 3!}w_3\right)\right)$$
$$=\left(\left(I_{0p}^{(3)}+I_{0L}^{(3)}+I_{0G}^{(3)}\right)\frac{\partial^2 w_0}{\partial t^2}+\left(I_{1p}^{(3)}+I_{1L}^{(3)}+I_{1G}^{(3)}\right)\frac{\partial^2 w_1}{\partial t^2}+\left(I_{2p}^{(3)}+I_{2L}^{(3)}+I_{2G}^{(3)}\right)\frac{\partial^2 w_2}{\partial t^2}+\left(I_{3p}^{(3)}+I_{3L}^{(3)}+I_{3G}^{(3)}\right)\frac{\partial^2 w_3}{\partial t^2}\right)$$
$$+=\left(\left(I_{0p}^{(3)}+I_{0L}^{(3)}+I_{0G}^{(3)}\right)\frac{\partial^2 w_0}{\partial t^2}+\left(I_{1p}^{(3)}+I_{1L}^{(3)}+I_{1G}^{(3)}\right)\frac{\partial^2 w_1}{\partial t^2}+\left(I_{2p}^{(3)}+I_{2L}^{(3)}+I_{2G}^{(3)}\right)\frac{\partial^2 w_2}{\partial t^2}+\left(I_{3p}^{(3)}+I_{3L}^{(3)}+I_{3G}^{(3)}\right)\frac{\partial^2 w_3}{\partial t^2}\right)$$
$$\left(\left(2V_LI_{0L}^{(3)}+2V_GI_{0G}^{(3)}\right)\frac{\partial^2 w_0}{\partial x\partial t}+\left(2V_LI_{1L}^{(3)}+2V_GI_{1G}^{(3)}\right)\frac{\partial^2 w_1}{\partial x\partial t}+\left(2V_LI_{2L}^{(3)}+2V_GI_{2G}^{(3)}\right)\frac{\partial^2 w_2}{\partial x\partial t}+\left(2V_LI_{3L}^{(3)}+2V_GI_{3G}^{(3)}\right)\frac{\partial^2 w_3}{\partial x\partial t}\right)$$
$$+\left(\left(V_L^2I_{0L}^{(3)}+V_G^2I_{0G}^{(3)}\right)\frac{\partial^2 w_0}{\partial x^2}+\left(V_L^2I_{1L}^{(3)}+V_G^2I_{1G}^{(3)}\right)\frac{\partial^2 w_1}{\partial x^2}+\left(V_L^2I_{2L}^{(3)}+V_G^2I_{2G}^{(3)}\right)\frac{\partial^2 w_2}{\partial x^2}+\left(V_L^2I_{3L}^{(3)}+V_G^2I_{3G}^{(3)}\right)\frac{\partial^2 w_3}{\partial x^2}\right) \tag{A12}$$

The corresponding boundary conditions are

$$\delta u_0 :\ \left(N_{xx}^{(0)}\right)\hat{n}_x+\left(\frac{N_{x\theta}^{(0)}}{R}\right)\hat{n}_\theta=0, \tag{A13}$$

$$\delta v_0 :\ \left(N_{x\theta}^{(0)}\right)\hat{n}_x+\left(\frac{N_{\theta\theta}^{(0)}}{R}\right)\hat{n}_\theta=0, \tag{A14}$$

$$\delta w_0 :\ \left(N_{xz}^{(0)}+N_{xx}^{(0)}\frac{\partial w_0}{\partial x}+\frac{N_{x\theta}^{(0)}}{2R}\frac{\partial w_0}{\partial \theta}\right)\hat{n}_x+\left(\frac{N_{\theta z}^{(0)}}{R}+\frac{N_{\theta\theta}^{(0)}}{R^2}\frac{\partial w_0}{\partial \theta}+\frac{N_{x\theta}^{(0)}}{2R}\frac{\partial w_0}{\partial x}\right)\hat{n}_\theta=0, \tag{A15}$$

$$\delta u_1 :\ \left(N_{xx}^{(1)}\right)\hat{n}_x+\left(\frac{N_{x\theta}^{(1)}}{R}\right)\hat{n}_\theta=0, \tag{A16}$$

$$\delta v_1 :\ \left(N_{x\theta}^{(1)}\right)\hat{n}_x+\left(\frac{N_{\theta\theta}^{(1)}}{R}\right)\hat{n}_\theta=0, \tag{A17}$$

$$\delta w_1 :\ \left(N_{xz}^{(1)}\right)\hat{n}_x+\left(\frac{N_{\theta z}^{(1)}}{R}\right)\hat{n}_\theta=0, \tag{A18}$$

$$\delta u_2 :\ \left(N_{xx}^{(2)}\right)\hat{n}_x+\left(\frac{N_{x\theta}^{(2)}}{R}\right)\hat{n}_\theta=0, \tag{A19}$$

$$\delta v_2 :\ \left(N_{x\theta}^{(2)}\right)\hat{n}_x+\left(\frac{N_{\theta\theta}^{(2)}}{R}\right)\hat{n}_\theta=0, \tag{A20}$$

$$\delta w_2 :\ \left(N_{xz}^{(2)}\right)\hat{n}_x+\left(\frac{N_{\theta z}^{(2)}}{R}\right)\hat{n}_\theta=0, \tag{A21}$$

$$\delta u_3 :\ \left(N_{xx}^{(3)}\right)\hat{n}_x+\left(\frac{N_{x\theta}^{(3)}}{R}\right)\hat{n}_\theta=0, \tag{A22}$$

$$\delta v_3 :\ \left(N_{x\theta}^{(3)}\right)\hat{n}_x+\left(\frac{N_{\theta\theta}^{(3)}}{R}\right)\hat{n}_\theta=0, \tag{A23}$$

$$\delta w_3 :\ \left(N_{xz}^{(3)}\right)\hat{n}_x+\left(\frac{N_{\theta z}^{(3)}}{R}\right)\hat{n}_\theta=0. \tag{A24}$$

where

$$\left\{N_{xx}^{(0)},N_{xx}^{(1)},N_{xx}^{(2)},N_{xx}^{(3)}\right\}=\int_{-\frac{h}{2}}^{\frac{h}{2}}\int_0^{2\pi}\int_0^{L}\left\{1,\frac{z}{1!},\frac{z^2}{2!},\frac{z^3}{3!}\right\}\sigma_{xx}Rdxd\theta dz, \tag{A25}$$

$$\left\{N_{\theta\theta}^{(0)},N_{\theta\theta}^{(1)},N_{\theta\theta}^{(2)},N_{\theta\theta}^{(3)}\right\}=\int_{-\frac{h}{2}}^{\frac{h}{2}}\int_0^{2\pi}\int_0^{L}\left\{1,\frac{z}{1!},\frac{z^2}{2!},\frac{z^3}{3!}\right\}\sigma_{\theta\theta}Rdxd\theta dz,$$

$$\left\{N_{zz}^{(0)},N_{zz}^{(1)},N_{zz}^{(2)},N_{zz}^{(3)}\right\}=\int_{-\frac{h}{2}}^{\frac{h}{2}}\int_0^{2\pi}\int_0^{L}\left\{1,\frac{z}{1!},\frac{z^2}{2!},\frac{z^3}{3!}\right\}\sigma_{zz}Rdxd\theta dz,$$

$$\left\{N_{xz}^{(0)}, N_{xz}^{(1)}, N_{xz}^{(2)}, N_{xz}^{(3)}\right\} = \int_{-\frac{h}{2}}^{\frac{h}{2}} \int_{0}^{2\pi} \int_{0}^{L} \left\{1, \frac{z}{1!}, \frac{z^2}{2!}, \frac{z^3}{3!}\right\} \tau_{xz} R dx d\theta dz,$$

$$\left\{N_{\theta z}^{(0)}, N_{\theta z}^{(1)}, N_{\theta z}^{(2)}, N_{\theta z}^{(3)}\right\} = \int_{-\frac{h}{2}}^{\frac{h}{2}} \int_{0}^{2\pi} \int_{0}^{L} \left\{1, \frac{z}{1!}, \frac{z^2}{2!}, \frac{z^3}{3!}\right\} \tau_{\theta z} R dx d\theta dz,$$

$$\left\{N_{x\theta}^{(0)}, N_{x\theta}^{(1)}, N_{x\theta}^{(2)}, N_{x\theta}^{(3)}\right\} = \int_{-\frac{h}{2}}^{\frac{h}{2}} \int_{0}^{2\pi} \int_{0}^{L} \left\{1, \frac{z}{1!}, \frac{z^2}{2!}, \frac{z^3}{3!}\right\} \tau_{x\theta} R dx d\theta dz,$$

$$\left\{I_{0p}^{(0)}, I_{1p}^{(0)}, I_{2p}^{(0)}, I_{3p}^{(0)}\right\} = \int_{-\frac{h}{2}}^{\frac{h}{2}} \int_{0}^{2\pi} \int_{0}^{L} \left\{1, \frac{z}{1!}, \frac{z^2}{2!}, \frac{z^3}{3!}\right\} \rho_p R dx d\theta dz,$$

$$\left\{I_{0p}^{(1)}, I_{1p}^{(1)}, I_{2p}^{(1)}, I_{3p}^{(1)}\right\} = \int_{-\frac{h}{2}}^{\frac{h}{2}} \int_{0}^{2\pi} \int_{0}^{L} \frac{z}{1!} \times \left\{1, \frac{z}{1!}, \frac{z^2}{2!}, \frac{z^3}{3!}\right\} \rho_p R dx d\theta dz,$$

$$\left\{I_{0p}^{(2)}, I_{1p}^{(2)}, I_{2p}^{(2)}, I_{3p}^{(2)}\right\} = \int_{-\frac{h}{2}}^{\frac{h}{2}} \int_{0}^{2\pi} \int_{0}^{L} \frac{z^2}{2!} \times \left\{1, \frac{z}{1!}, \frac{z^2}{2!}, \frac{z^3}{3!}\right\} \rho_p R dx d\theta dz,$$

$$\left\{I_{0p}^{(3)}, I_{1p}^{(3)}, I_{2p}^{(3)}, I_{3p}^{(3)}\right\} = \int_{-\frac{h}{2}}^{\frac{h}{2}} \int_{0}^{2\pi} \int_{0}^{L} \frac{z^3}{3!} \times \left\{1, \frac{z}{1!}, \frac{z^2}{2!}, \frac{z^3}{3!}\right\} \rho_p R dx d\theta dz,$$

$$\left\{I_{0L}^{(0)}, I_{1L}^{(0)}, I_{2L}^{(0)}, I_{3L}^{(0)}\right\} = \int_{-\frac{h}{2}-R_i}^{-\frac{h}{2}} \int_{0}^{2\pi} \int_{0}^{L} \left\{1, \frac{z}{1!}, \frac{z^2}{2!}, \frac{z^3}{3!}\right\} \rho_L R dx d\theta dz,$$

$$\left\{I_{0L}^{(1)}, I_{1L}^{(1)}, I_{2L}^{(1)}, I_{3L}^{(1)}\right\} = \int_{-\frac{h}{2}-R_i}^{-\frac{h}{2}} \int_{0}^{2\pi} \int_{0}^{L} \frac{z}{1!} \times \left\{1, \frac{z}{1!}, \frac{z^2}{2!}, \frac{z^3}{3!}\right\} \rho_L R dx d\theta dz,$$

$$\left\{I_{0L}^{(2)}, I_{1L}^{(2)}, I_{2L}^{(2)}, I_{3L}^{(2)}\right\} = \int_{-\frac{h}{2}-R_i}^{-\frac{h}{2}} \int_{0}^{2\pi} \int_{0}^{L} \frac{z^2}{2!} \times \left\{1, \frac{z}{1!}, \frac{z^2}{2!}, \frac{z^3}{3!}\right\} \rho_L R dx d\theta dz,$$

$$\left\{I_{0L}^{(3)}, I_{1L}^{(3)}, I_{2L}^{(3)}, I_{3L}^{(3)}\right\} = \int_{-\frac{h}{2}-R_i}^{-\frac{h}{2}} \int_{0}^{2\pi} \int_{0}^{L} \frac{z^3}{3!} \times \left\{1, \frac{z}{1!}, \frac{z^2}{2!}, \frac{z^3}{3!}\right\} \rho_L R dx d\theta dz,$$

$$\left\{I_{0G}^{(0)}, I_{1G}^{(0)}, I_{2G}^{(0)}, I_{3G}^{(0)}\right\} = \int_{-\frac{h}{2}-R_i}^{-\frac{h}{2}} \int_{0}^{2\pi} \int_{0}^{L} \left\{1, \frac{z}{1!}, \frac{z^2}{2!}, \frac{z^3}{3!}\right\} \rho_G R dx d\theta dz,$$

$$\left\{I_{0G}^{(1)}, I_{1G}^{(1)}, I_{2G}^{(1)}, I_{3G}^{(1)}\right\} = \int_{-\frac{h}{2}-R_i}^{-\frac{h}{2}} \int_{0}^{2\pi} \int_{0}^{L} \frac{z}{1!} \times \left\{1, \frac{z}{1!}, \frac{z^2}{2!}, \frac{z^3}{3!}\right\} \rho_G R dx d\theta dz,$$

$$\left\{I_{0G}^{(2)}, I_{1G}^{(2)}, I_{2G}^{(2)}, I_{3G}^{(2)}\right\} = \int_{-\frac{h}{2}-R_i}^{-\frac{h}{2}} \int_{0}^{2\pi} \int_{0}^{L} \frac{z^2}{2!} \times \left\{1, \frac{z}{1!}, \frac{z^2}{2!}, \frac{z^3}{3!}\right\} \rho_G R dx d\theta dz,$$

$$\left\{I_{0G}^{(3)}, I_{1G}^{(3)}, I_{2G}^{(3)}, I_{3G}^{(3)}\right\} = \int_{-\frac{h}{2}-R_i}^{-\frac{h}{2}} \int_{0}^{2\pi} \int_{0}^{L} \frac{z^3}{3!} \times \left\{1, \frac{z}{1!}, \frac{z^2}{2!}, \frac{z^3}{3!}\right\} \rho_G R dx d\theta dz.$$

Data availability

Data will be made available on request.

References

[1] X. Zhang, W. Zhang, X. ZHANG, T. LEI, Experimental research on aero-propulsion coupling characteristics of a distributed electric propulsion aircraft, Chinese Journal of Aeronautics 36 (2023) 201–212.
[2] S. Pheasant, CM. Haslegrave, Bodyspace: Anthropometry, ergonomics and the design of work, CRC press, 2018.
[3] H. Kim, Y. Nam, Condensation behaviors and resulting heat transfer performance of nano-engineered copper surfaces, Int. J. Heat. Mass Transf. 93 (2016) 286–292.
[4] MK. Smart, Flow modeling of pseudoshocks in backpressured ducts, AIAA Journal 53 (2015) 3577–3588.
[5] AM. Brown, Structural Dynamics Applied to Rocket Engine Turbopumps. Structural Dynamics of Liquid Rocket Engines: A Holistic Approach, Springer, 2023, pp. 67–114.
[6] B.F. Porto, Souto C d'Andrade, Dynamic analysis of a liquid rocket turbo-pump (2011).
[7] T. Zhong, K. He, H. Li, L. Yang, Mechanical properties of lightweight 316L stainless steel lattice structures fabricated by selective laser melting, Mater. Des. 181 (2019) 108076.
[8] D. Qi, H. Yu, M. Liu, H. Huang, S. Xu, Y. Xia, et al., Mechanical behaviors of SLM additive manufactured octet-truss and truncated-octahedron lattice structures with uniform and taper beams, Int. J. Mech. Sci. 163 (2019) 105091.
[9] M. Sadeghzade, H. Gharehbaghi, A. Farrokhabadi, Experimental and analytical studies of mechanical properties of additively manufactured lattice structure based on octagonal bipyramid cubic unit cell, Addit. Manuf. 48 (2021) 102403.
[10] X. Cao, S. Duan, J. Liang, W. Wen, D. Fang, Mechanical properties of an improved 3D-printed rhombic dodecahedron stainless steel lattice structure of variable cross section, Int. J. Mech. Sci. 145 (2018) 53–63.
[11] L. Xiao, W. Song, C. Wang, H. Tang, Q. Fan, N. Liu, et al., Mechanical properties of open-cell rhombic dodecahedron titanium alloy lattice structure manufactured using electron beam melting under dynamic loading, Int. J. Impact. Eng. 100 (2017) 75–89.
[12] M. Lai, A.N. Kulak, D. Law, Z. Zhang, F.C. Meldrum, DJ. Riley, Profiting from nature: macroporous copper with superior mechanical properties, Chemical Communications (2007) 3547–3549.
[13] L. Wu, W. Wang, W. Zhang, H. Su, J. Gu, Q. Liu, et al., Optical Performance Study of Gyroid-Structured TiO2 Photonic Crystals Replicated from Natural Templates using a Sol-Gel Method, Adv. Opt. Mater. 6 (2018) 1800064.
[14] X. Li, L. Xiao, W. Song, Compressive behavior of selective laser melting printed Gyroid structures under dynamic loading, Addit. Manuf. 46 (2021) 102054.
[15] S. AlMahri, R. Santiago, D-W Lee, H. Ramos, H. Alabdouli, M. Alteneiji, et al., Evaluation of the dynamic response of triply periodic minimal surfaces subjected to high strain-rate compression, Addit. Manuf. 46 (2021) 102220.
[16] N. Novak, O. Al-Ketan, L. Krstulović-Opara, R. Rowshan, Al-Rub RKA, M. Vesenjak, et al., Quasi-static and dynamic compressive behaviour of sheet TPMS cellular structures, Compos. Struct. 266 (2021) 113801.
[17] Y. Wang, X. Ren, Z. Chen, Y. Jiang, X. Cao, S. Fang, et al., Numerical and experimental studies on compressive behavior of Gyroid lattice cylindrical shells, Mater. Des. 186 (2020) 108340.
[18] Q. Sun, J. Sun, K. Guo, L. Wang, Compressive mechanical properties and energy absorption characteristics of SLM fabricated Ti6Al4V triply periodic minimal surface cellular structures, Mechanics of Materials 166 (2022) 104241.
[19] H. Yin, Z. Liu, J. Dai, G. Wen, C. Zhang, Crushing behavior and optimization of sheet-based 3D periodic cellular structures, Composites Part B: Engineering 182 (2020) 107565.
[20] K.Q. Tran, T.D. Le, N.V. Nguyen, H. Nguyen-Xuan, Design of 3D rotating triply periodic minimal surface (RotTPMS) lattice plates: Meanings of crystalline rotations and porosity, Int. J. Mech. Sci. 270 (2024) 109090.
[21] A.O. Oyelade, AA. Oyediran, Nonlinear dynamics of horizontal pipes conveying two phase flow, European Journal of Mechanics-A/Solids 90 (2021) 104367.
[22] O. Orozovic, A. Lavrinec, H. Rajabnia, K. Williams, M. Jones, G. Klinzing, Transport boundaries and prediction of the slug velocity and layer fraction in horizontal slug flow pneumatic conveying, Chem. Eng. Sci. 227 (2020) 115916.
[23] C. An, J. Su, Dynamic behavior of pipes conveying gas–liquid two-phase flow, Nuclear Engineering and Design 292 (2015) 204–212.
[24] Y. Modarres-Sadeghi, MP. Païdoussis, Chaotic oscillations of long pipes conveying fluid in the presence of a large end-mass, Comput. Struct. 122 (2013) 192–201.
[25] S. Li, B.W. Karney, G. Liu, FSI research in pipeline systems–A review of the literature, J. Fluids. Struct. 57 (2015) 277–297.
[26] MP. Païdoussis, Pipes conveying fluid: a fertile dynamics problem, J. Fluids. Struct. 114 (2022) 103664.
[27] Y. Liu, S. Miwa, T. Hibiki, M. Ishii, H. Morita, Y. Kondoh, et al., Experimental study of internal two-phase flow induced fluctuating force on a 90 elbow, Chem. Eng. Sci. 76 (2012) 173–187.
[28] J-L Riverin, MJ. Pettigrew, Vibration excitation forces due to two-phase flow in piping elements (2007).
[29] C. Monette, MJ. Pettigrew, Fluidelastic instability of flexible tubes subjected to two-phase internal flow, J. Fluids. Struct. 19 (2004) 943–956.
[30] F. Li, C. An, M. Duan, J. Su, Combined damping model for dynamics and stability of a pipe conveying two-phase flow, Ocean Engineering 195 (2020) 106683.
[31] M. Cargnelutti, S. Belfroid, W. Schiferli, Two-phase flow-induced forces on bends in small scale tubes (2010).
[32] S. Miwa, M. Mori, T. Hibiki, Two-phase flow induced vibration in piping systems, Progress in Nuclear Energy 78 (2015) 270–284.
[33] A. Ebrahimi-Mamaghani, R. Sotudeh-Gharebagh, R. Zarghami, N. Mostoufi, Dynamics of two-phase flow in vertical pipes, J. Fluids. Struct. 87 (2019) 150–173.
[34] M. Chehreghani, A. Shaaban, A.K. Misra, MP. Païdoussis, Dynamics of a hanging fluid-discharging pipe subjected to reverse external flow: an experimental investigation, J. Fluids. Struct. 119 (2023) 103889.
[35] Y. Ma, Y. You, K. Chen, L. Hu, A. Feng, Application of harmonic differential quadrature (HDQ) method for vibration analysis of pipes conveying fluid, Appl. Math. Comput. 439 (2023) 127613.
[36] Y. Ma, D. Zhou, Y. You, Y. Shen, K. Chen, A. Feng, Stability analysis for internal flow-induced vertical cantilevered pipe subject to multiple lumped masses, J. Fluids. Struct. 120 (2023) 103896.
[37] B. Lu, Y. Xia, Y. Ren, M. Xie, L. Zhou, G. Vinai, et al., When Machine Learning Meets 2D Materials: A Review, Advanced Science 11 (2024) 2305277.
[38] L. Sun, T. Liang, C. Zhang, J. Chen, The rheological performance of shear-thickening fluids based on carbon fiber and silica nanocomposite, Physics of Fluids 35 (2023).
[39] Y. Su, Z. Shen, X. Long, C. Chen, L. Qi, X. Chao, Gaussian filtering method of evaluating the elastic/elasto-plastic properties of sintered nanocomposites with quasi-continuous volume distribution, Materials Science and Engineering: A 872 (2023) 145001.
[40] Y. ZHAO, J. JING, L. CHEN, F. XU, H. HOU, Current research status of interface of ceramic-metal laminated composite material for armor protection, Acta Metall Sin 57 (2021) 1107–1125.
[41] I. Maskery, L. Sturm, A.O. Aremu, A. Panesar, C.B. Williams, C.J. Tuck, et al., Insights into the mechanical properties of several triply periodic minimal surface lattice structures made by polymer additive manufacturing, Polymer. (Guildf) 152 (2018) 62–71.
[42] H. Nguyen-Xuan, K.Q. Tran, C.H. Thai, J. Lee, Modelling of functionally graded triply periodic minimal surface (FG-TPMS) plates, Compos. Struct. 315 (2023) 116981.
[43] S.M. Bhagwat, AJ. Ghajar, A flow pattern independent drift flux model based void fraction correlation for a wide range of gas–liquid two phase flow, International Journal of Multiphase Flow 59 (2014) 186–205.
[44] A. Ebrahimi-Mamaghani, N. Mostoufi, R. Sotudeh-Gharebagh, R. Zarghami, Vibrational analysis of pipes based on the drift-flux two-phase flow model, Ocean Engineering 249 (2022) 110917.
[45] MH. Sadd, Elasticity: theory, applications, and numerics, Academic Press, 2009.
[46] R. Mohammadi, M. Hosseini, Modeling and free vibration analysis of a rotating functionally graded thin-walled hub-blade system under aerothermoelastic loading, Aerosp. Sci. Technol. 146 (2024) 108935, https://doi.org/10.1016/j.ast.2024.108935.
[47] T.Q. Quan, V.M. Anh, ND. Duc, Natural frequency analysis of sandwich plate with auxetic honeycomb core and CNTRC face sheets using analytical approach and artificial neural network, Aerosp. Sci. Technol. 144 (2024) 108806, https://doi.org/10.1016/j.ast.2023.108806.
[48] X. Li, J. Li, Y. Li, M. Li, Nonlinear dynamic modelling and analysis of a rotating composite thin-walled beam considering ice coating, Aerosp. Sci. Technol. 148 (2024) 109086, https://doi.org/10.1016/j.ast.2024.109086.
[49] A. Behravanrad, M. Jafari, Thermo-mechanical behavior of 2D functionally graded porous-auxetic metamaterial rotating disk with an auxetic foundation, Aerosp. Sci. Technol. 145 (2024) 108829, https://doi.org/10.1016/j.ast.2023.108829.
[50] EH. Dowell, Nonlinear oscillations of a fluttering plate, AIAA Journal 4 (1966) 1267–1275.
[51] EH. Dowell, Panel flutter-A review of the aeroelastic stability of plates and shells, AIAA Journal 8 (1970) 385–399.
[52] K. Zhou, J. Su, H. Hua, Aero-thermo-elastic flutter analysis of supersonic moderately thick orthotropic plates with general boundary conditions, Int. J. Mech. Sci. 141 (2018) 46–57.
[53] L. Sun, Y.X. Hao, W. Zhang, H. Li, Traveling wave vibration and critical rotating speed of rotating porous metal conical shell with elastic boundary conditions, Aerosp. Sci. Technol. 148 (2024) 109091, https://doi.org/10.1016/j.ast.2024.109091.
[54] Z. Pan, J. Cheng, L. Zhao, AE. Ragab, Thermo-dynamic response of multi-directional functionally graded panels resting on an elastic substrate with the aid of data-driven solution, Aerosp. Sci. Technol. 143 (2023) 108724, https://doi.org/10.1016/j.ast.2023.108724.
[55] P.H. Wan, M.S.H. Al-Furjan, R. Kolahchi, Nonlinear flutter response and reliability of supersonic smart hybrid nanocomposite rupture trapezoidal plates subjected to yawed flow using DQHFEM, Aerosp. Sci. Technol. 145 (2024) 108862, https://doi.org/10.1016/j.ast.2023.108862.
[56] A. Rahimi, A. Alibeigloo, M. Safarpour, Three-dimensional static and free vibration analysis of graphene platelet–reinforced porous composite cylindrical shell, Journal of Vibration and Control 26 (2020) 1627–1645, https://doi.org/10.1177/1077546320902340.

[57] F. Tornabene, N. Fantuzzi, F. Ubertini, E. Viola, Strong formulation finite element method based on differential quadrature: a survey, Appl. Mech. Rev. 67 (2015).
[58] M. Mirzaei, Y. Kiani, Nonlinear free vibration of temperature-dependent sandwich beams with carbon nanotube-reinforced face sheets, Acta Mech. 227 (2016) 1869–1884.
[59] M. Ishii, T. Hibiki, Thermo-fluid dynamics of two-phase flow, Springer Science & Business Media, 2010.
[60] T. Ozaki, T. Hibiki, Drift-flux model for rod bundle geometry, Progress in Nuclear Energy 83 (2015) 229–247.
[61] M. Kaichiro, M. Ishii, Flow regime transition criteria for upward two-phase flow in vertical tubes, Int. J. Heat. Mass Transf. 27 (1984) 723–737.
[62] H. Zhang, T. Hibiki, Y. Xiao, H. Gu, Two-group drift-flux model in tight lattice subchannel, International Communications in Heat and Mass Transfer 159 (2024) 108201.
[63] GB. Wallis, One-dimensional two-phase flow, Courier Dover Publications, 2020.
[64] M.C. Ozden, U. Simsek, M. Ozdemir, C.E. Gayir, P. Sendur, Innovative Vibration Control of Triply Periodic Minimum Surfaces Lattice Structures: A Hybrid Approach with Constrained Layer Damping Silicone–Viscoelastic Layer Integration, Adv. Eng. Mater. 26 (2024) 2401851.
[65] Y.H. Dong, B. Zhu, Y. Wang, Y.H. Li, J. Yang, Nonlinear free vibration of graded graphene reinforced cylindrical shells: Effects of spinning motion and axial load, J. Sound. Vib. 437 (2018) 79–96, https://doi.org/10.1016/j.jsv.2018.08.036.
[66] F. Pellicano, Vibrations of circular cylindrical shells: theory and experiments, J. Sound. Vib. 303 (2007) 154–170.